



HAL
open science

Experimentally determined Si isotope fractionation between zircon and quartz

Dustin Trail, Paul Savage, Frédéric Moynier

► **To cite this version:**

Dustin Trail, Paul Savage, Frédéric Moynier. Experimentally determined Si isotope fractionation between zircon and quartz. *Geochimica et Cosmochimica Acta*, 2019, 260, pp.257-274. 10.1016/j.gca.2019.06.035 . insu-02916949

HAL Id: insu-02916949

<https://insu.hal.science/insu-02916949>

Submitted on 19 Aug 2020

HAL is a multi-disciplinary open access archive for the deposit and dissemination of scientific research documents, whether they are published or not. The documents may come from teaching and research institutions in France or abroad, or from public or private research centers.

L'archive ouverte pluridisciplinaire **HAL**, est destinée au dépôt et à la diffusion de documents scientifiques de niveau recherche, publiés ou non, émanant des établissements d'enseignement et de recherche français ou étrangers, des laboratoires publics ou privés.

1 *submitted to GCA*

2
3
4
5 Experimentally determined Si isotope
6 fractionation between zircon and quartz
7

8
9
10 Dustin Trail¹, Paul S. Savage² and Frédéric Moynier^{3,4}
11

12
13 ¹Department of Earth & Environmental Sciences, University of Rochester, Rochester, NY
14 14627, USA.

15 ²School of Earth and Environmental Sciences, University of St Andrews, Irvine Building,
16 Scotland, UK, KY16 9AL

17 ³Université de Paris, Institut de physique du globe de Paris, CNRS, F-75005 Paris, France

18 ⁴Institut Universitaire de France, Paris, France
19

20 Corresponding author: Dustin Trail (dtrail@ur.rochester.edu)
21

22 *Submitted Feb 9th 2019*

23 *Revised June 20th, 2019*
24
25
26
27

28 Keywords Si isotopes; fractionation; igneous; zircon; quartz; three-isotope

29 **Abstract.** The silicon isotope composition of detrital quartz and zircon have the potential to
30 inform us about secular changes to the silica cycle and weathering reactions on Earth. However,
31 inferring source melt Si isotope composition from out-of-context minerals is hampered by the
32 fact that, to-date, there is limited Si isotope equilibrium fractionation data for minerals. Here, we
33 report experimental data to constrain Si isotope equilibrium fractionation between zircon and
34 quartz, using two fundamentally different strategies, but with the same experimental design.
35 First, zircon and quartz were hydrothermally synthesized from $Zr(OH)_4$ and SiO_2 at 1.5 GPa and
36 temperatures of 725, 800, and 900 °C. The second experimental strategy utilized the three-
37 isotope method; the starting materials consisted of natural zircon and isotopically-labelled SiO_2 .
38 Three sets of hydrothermal time-series experiments were conducted at the same pressure and
39 temperatures as the direct synthesis experiments. For all experiments, quartz and zircon were
40 separated and $^{30}Si/^{28}Si$ and $^{29}Si/^{28}Si$ ratios were measured by solution multi-collector inductively
41 coupled plasma mass spectrometry. The three-isotope method, which provides the best indicator
42 of equilibrium fractionations, yields the following relationship:

43

$$44 \Delta^{30}Si(qtz-zrc) = (0.53 \pm 0.14) \times 10^6 / T^2$$

45

46 where $\Delta^{30}Si(qtz-zrc)$ is the relative difference in $^{30}Si/^{28}Si$ between quartz and zircon in permil, T
47 is temperature in K, and the error is 2 s.e. This relationship can be used to calculate the
48 fractionation between zircon and other phases, and to estimate the Si isotope composition of the
49 melt from which a zircon crystallized. The results may be used to assess equilibrium-
50 disequilibrium isotope fractionations between quartz and zircon and co-existing phases in
51 igneous rocks. These data can also be applied to out-of-context zircon (and quartz) to estimate
52 the isotope composition of the host rock. Zircons crystallizing from a melt derived from purely
53 igneous sources – i.e., without the involvement of “weathered” material – are expected to display
54 a $\delta^{30}Si_{NBS-28}$ (permil deviation of the $^{30}Si/^{28}Si$ from the NBS-28 standard) range from -0.7 to -
55 0.35‰. Deviations from this range indicate assimilation of non-igneous (i.e., sedimentary)
56 material in the melt source.

57

58

59

60

61

62

63

64

65

66

67

68

69

70

71

72

73

74

75

76 1. Introduction

77

78 The processes of silicate weathering and assimilation of sedimentary material into crustal
79 melts have been explored in detail through measurements of oxygen isotope ratios in whole rock
80 for over 50 years (Taylor, 1968; Taylor and Sheppard, 1986). This is because oxygen isotope
81 ratios of supracrustal and aqueously-altered rocks are fractionated away from the canonical
82 mantle value (O'Neil and Chappell, 1977; Harmon and Hoefs, 1995). Anatexis of such altered
83 material during the formation of melt thus yields different bulk-rock $^{18}\text{O}/^{16}\text{O}$ ratios when
84 compared to primitive mantle-derived magmas. In most cases, supracrustal contamination yields
85 igneous rocks enriched in ^{18}O compared to the upper mantle, because weathering results in
86 relatively large enrichment in the heavy isotopes of the weathered rocks (Savin and Epstein,
87 1970). Trends to $^{18}\text{O}/^{16}\text{O}$ values lower than mantle may occur by assimilation of high-
88 temperature, hydrothermally-altered material caused by a change in the fractionation direction
89 vs. temperature during chemical weathering (e.g. Wenner and Taylor, 1973; Chacko et al., 2001),
90 or by assimilation of material altered by meteoric water (e.g., Bindeman et al., 2007).

91 Using oxygen isotopes as a proxy for supracrustal contamination in igneous systems at
92 the mineral-scale requires knowledge of the direction and magnitude of O isotope fractionation
93 among phases. Experimentally-, empirically, and theoretically-derived mineral-mineral oxygen
94 isotope fractionations (Keiffer, 1982; Mathews et al., 1983; Chiba et al., 1989; Chacko et al.,
95 2001; Trail et al., 2009) have resulted in a clearer understanding of the relationship between
96 crustal weathering, recycling, and the isotopic composition recorded in individual igneous
97 phases. One phase that has offered many important insights is zircon, which is generally
98 unaffected by chemical weathering (e.g., Valley et al., 1994; 2003; Grimes et al., 2013; Loewen
99 and Bindeman, 2015, 2016) and can be dated by U-Pb geochronology (Harrison et al., 2017). For
100 instance, some zircons older than 4.0 Ga have oxygen isotope compositions that are enriched in
101 ^{18}O relative to mantle zircon (Valley et al., 1998; Cavosie et al., 2009), providing evidence for
102 low-temperature fluid alteration of their protoliths and suggesting that significant volumes of
103 liquid water were interacting with the crust as early as 4.2 to 4.3 Ga (Mojzsis et al., 2001;
104 Cavosie et al., 2005).

105 Other isotope tracers, such as $^7\text{Li}/^6\text{Li}$ and $^{26}\text{Mg}/^{24}\text{Mg}$, have been used with success to
106 study silicate weathering (e.g. Teng et al., 2010, Wimpenny et al., 2011) though perhaps no other
107 isotope system is more important than Si due its pervasive abundance in the lithosphere and
108 weathered products. Silicon isotopes, like oxygen isotopes, fractionate away from igneous
109 compositions during weathering in many low-temperature water-rock interactions, particularly
110 during desilicification and neof ormation of clay minerals (Opfergelt et al., 2012; Savage et al.,
111 2013). There is also evidence that a supracrustal Si isotope signature can be transferred to a melt;
112 depletions in the light isotopes of Si were detected in several peraluminous leucogranites
113 (Poitrasson and Zambardi, 2015). Savage et al. (2012) also identified measurable differences in
114 the Si isotopic composition of igneous rocks from the Lachlan Fold Belt, Australia, which
115 revealed new information about the source materials of these (S)edimentary- and (I)gneous- type
116 granitoids. Specifically, Ordovician sediments near these granitoids are often interpreted to
117 represent the supracrustal end-member for the S-type rocks (e.g., Keay et al., 1997), yet Si
118 isotope compositions strongly suggest that these sediments were not the only source of material
119 (Savage et al., 2012); pre-Ordovician metasedimentary crust may have also contributed to the
120 isotopic character of the LFB granitoids (Chappell et al., 1988).

121 Studies have also coupled Si and O isotope ratios to infer that Si from marine
122 hydrothermal origin and a minor fraction from continental weathering contributed to the
123 chemistry of banded iron formations, as early as 3.8 Ga (Heck et al., 2011). More recently, new
124 insights into the terrestrial silica cycle and weathering reactions prior to 3.8 Ga have been
125 gleaned from coupled Si and O isotope measurements of Archean and Hadean detrital zircons
126 (Trail et al., 2018). These data provide evidence for the presence (and subsequent melting) of
127 fluid-altered, crustal assemblages such as serpentinites and possibly authigenic silica on the
128 Hadean Earth.

129 As with O isotopes, the direction and magnitude of Si isotope high temperature
130 fractionations among co-existing igneous phases needs to be well constrained so that the bulk-
131 rock Si isotope composition can be confidently inferred, particularly when *ex-situ* mineral phases
132 are analyzed. This will allow for any signature of supracrustal material in the melt source to be
133 better elucidated via this isotope system. The importance of this is amplified because Si isotope
134 fractionations produced during weathering or low temperature hydrothermal processes are
135 typically smaller in magnitude than O isotopes. The Si isotope composition of clays, for
136 example, are typically confined to -0.5 to -3 ‰ (relative difference when compared to the mantle
137 frame of reference; Opfergelt et al., 2012), though Bayon et al. (2018) showed that a small
138 fraction of clays can in be isotopically unfractionated relative to average (unweathered) felsic
139 crustal composition. In comparison, clay mineral ¹⁸O/¹⁶O ratios with differences of +10 ‰
140 compared to the mantle frame of reference are common (Savin and Epstein, 1970; Chacko et al.,
141 2001).

142 Variations in $\delta^{30}\text{Si}$ between natural igneous mineral assemblages have been measured in
143 previous studies (Savage et al. 2011, 2012), where $\delta^{30}\text{Si}$ is defined as the permil difference of the
144 $^{30}\text{Si}/^{28}\text{Si}$ ratio of the sample relative to the same ratio in NBS-28 silica sand, as follows:

$$146 \quad \delta^{30}\text{Si} = \left[\frac{^{30}\text{Si}/^{28}\text{Si}_{\text{sample}}}{^{30}\text{Si}/^{28}\text{Si}_{\text{NBS-28}}} - 1 \right] \times 1000 \quad (1).$$

147 Silicon isotope mineral-mineral fractionations at igneous temperatures are typically range from
148 0.05 – 0.50 ‰ (Savage et al., 2012; and Trail et al., 2018), though density functional theory
149 (DFT) calculations predict quartz-clinopyroxene (i.e., diopside and clinoenstatite) fractionations
150 that approach or exceed 0.5 ‰ (1000 K; Méheut et al., 2009; Qin et al., 2016). The direction and
151 magnitude of fractionation is thought to be controlled by the relative degree of polymerization of
152 the minerals. Restated, phases with higher proportions of Si-O-Si bonds tend to prefer the
153 heavier Si isotopes (e.g., Méheut et al., 2009; Savage et al., 2011); i.e., orthosilicates (e.g.,
154 olivine) are almost always isotopically lighter than tectosilicates (e.g., feldspar).

156 Due to the orthosilicate structure of zircon, it is predicted that zircon should be
157 isotopically light, particularly if crystallizing from a high silica melt where most liquidus phases
158 are tectosilicates (Qin et al., 2016). Quartz, on the other hand, should be enriched in the heavy
159 isotopes of Si. This was confirmed by Trail et al. (2018), who measured zircon-quartz
160 fractionation values for an aliquot of zircon and quartz from the I-type Jindabyne tonalite, from
161 the Lachlan Fold Belt (LFB), Australia (Trail et al., 2017). A fractionation of $\delta^{30}\text{Si}(\text{qtz}) -$
162 $\delta^{30}\text{Si}(\text{zrc}) = \Delta^{30}\text{Si}(\text{qtz-zrc}) = 0.47 \pm 0.06 \text{ ‰}$ ($T_{\text{cryst}} \sim 750 \text{ °C}$) was measured via multi-collector
163 inductively-coupled-plasma mass-spectrometry (MC-ICP-MS). These measurements also agree
164 with DFT calculations for analogous mineral pairs. That is, quartz-pyrope fractionations (pyrope
165 being an orthosilicate) are equal to 0.48 ‰ at 750 °C (Méheut and Schauble, 2014).

166 However, there are some important caveats for the above generalizations. Firstly, implicit
167 in constraining a fractionation from natural samples is the assumption that zircon and quartz
168 crystallized contemporaneously and in equilibrium, which may or may not be the case.
169 Secondly, it is not clear to what extent the predicted polymerization-related fractionation rule
170 holds when other network-modifying cations, such as Al, OH⁻, B are present in high abundances
171 in the melt and crystallizing phases. The control of relative polymerization on Si isotope
172 fractionation is clearly not a consistent phenomenon, as both empirical measurements and first
173 principle DFT calculations imply that olivine is isotopically heavier than coexisting
174 clinoenstatite, despite having more “non-bridging” oxygens (Méheut et al., 2009; Savage et al.,
175 2011). Moreover, measured fractionations between quartz and biotite/phlogopite (Ding et al.
176 1996; Georg, 2006) are lighter than would be expected by a applying the simple polymerization
177 rule for the three corner-sharing structure of trioctahedral phyllosilicates (Méheut and Schauble,
178 2014). Zircon also exhibits unique properties among the silicate minerals whose fractionations
179 were calculated by DTF (Qin et al., 2016). That is, its calculated ³⁰Si/²⁸Si reduced partition
180 function ratio vs. Si-O polyhedron volume is well outside the trend identified for other silicates,
181 which is due to a large distortion in the zircon silica tetrahedron (Qin et al., 2016). Thirdly, even
182 I-type granitoids are known to contain inherited zircons (e.g., Kemp et al., 2005), which means
183 that the natural quartz-zircon fractionation noted above could be affected by a mixture of
184 multiple zircon populations. Finally, stable isotope fractionation is a temperature-dependent
185 process. Constraining the sensitivity of Δ³⁰Si(qtz-zrc) to crystallization temperature is critical to
186 accurately infer whole-rock/melt compositions from out-of-context minerals.

187 Thus, there is a need to approach the topic of igneous Si isotope fractionation between
188 zircon and whole-rock/coexisting minerals in a systematic and controlled fashion. While several
189 studies have conducted calculations to constrain Si isotope fractionations among coexisting
190 minerals and fluids (Méheut et al., 2007, 2009; Méheut and Schauble, 2014; Huang et al., 2014;
191 Qin et al., 2016), we aware of no experimental Si isotope fractionation data for igneous minerals.
192 We present high temperature Si isotope fractionation experiments between zircon and quartz by
193 direct synthesis, and through application of the three-isotope method (e.g. Matsuhisa et al., 1978;
194 Shahar et al., 2008; Macris et al., 2013), to place inferences made from zircon Si isotope
195 measurements in a more complete context. We show that the direction of experimentally
196 determined Si isotope quartz-zircon fractionations agrees with natural and theoretical data (Qin
197 et al., 2016; Trail et al., 2018), though some differences in the magnitude are observed. When
198 experimentally determined quartz-zircon fractionations are combined with measurements
199 collected on natural samples, we also show that the Si isotopic difference between zircon and
200 whole rock can be confidently estimated in simplified scenarios.

201

202

203 **2. Methods**

204

205 **2.1 Experimental strategy and design**

206

207 High temperature Si isotope fractionations – in this case quartz and zircon – are typically
208 described by the following relationship:

209

$$210 \delta^{30}\text{Si}(\text{qtz}) - \delta^{30}\text{Si}(\text{zrc}) = \Delta^{30}\text{Si}(\text{qtz} - \text{zrc}) \cong 10^3 \times \ln(\alpha_{\text{qtz-zrc}}) = \frac{A \times 10^6}{T^2} (2)$$

211

212 where T is in K, and $\alpha_{qtz-zrc}$ is the fractionation factor defined by the $^{30}\text{Si}/^{28}\text{Si}$ value in quartz
213 divided by the equivalent ratio in zircon, and A is a constant parameter. This relationship is
214 typically assumed to be a valid description of high temperature (≥ 500 °C) isotope fractionations
215 (Bottinga and Javoy, 1973). While polynomial expressions such as $10^3 \ln(\alpha_{\text{mineral1-mineral2}}) = Ax -$
216 $Bx^2 + Cx^3$ – where $x=10^6/T^2$ – are frequently used for theoretical calibrations (e.g., Qin et al.,
217 2016), such functions are rarely used for high temperature experimental or naturally-calibrated
218 fractionation studies because the obtained fractionations are typically not precise enough to
219 resolve the B - and C -values. For the data presented here, we utilize equation (2) which implies
220 an assumed linearity for $\Delta^{30}\text{Si}(qtz-zrc)$ vs. $1/T^2$, that $\alpha_{qtz-zrc}$ is close to 1, and that A can be solved
221 for by knowing T and the Si isotope compositions of quartz and zircon. We conducted a series
222 of fluid-saturated experiments in a piston cylinder device to characterize the A -value using two
223 different experimental designs.

224

225 2.1.1 Direct synthesis experiments

226

227 We performed direct synthesis experiments of zircon and quartz with starting materials
228 consisting of $\text{Zr}(\text{OH})_4$, SiO_2 , and a 10 mM CaCl_2 solution. The SiO_2 consisted of 325 mesh
229 fused ~amorphous powder from Alfa Aesar with a stated purity of 99.8%. The $\text{Zr}(\text{OH})_4$ was
230 made by first dissolving 99.9% pure ZrCl_4 from Sigma Aldrich in distilled water under a fume
231 hood; a $\text{Zr}(\text{OH})_4$ gel was precipitated by adding NH_4OH to this solution (Montel et al., 1989;
232 Trail et al., 2011). The gel was carefully rinsed, left to sit at room temperature until dry, and
233 then ground. A 10 mM CaCl_2 solution was made by dissolving $\text{CaCl}_2 \cdot 2\text{H}_2\text{O}$ (99% purity, Alfa
234 Aesar) and trace DyCl_3 (99.99% purity; Sigma Aldrich) in distilled water.

235 The SiO_2 and $\text{Zr}(\text{OH})_4$ were weighed out for each individual experiment in 2:1
236 abundances by mole, for a total mass of ~70 mg. This material was coarsely mixed by hand in
237 the weighing paper with a spatula before loading it into a 4.8 mm diameter capsule machined
238 from an Ag rod with an outer diameter of 7.3 mm. Approximately 60 μL of 10 mM CaCl_2
239 solution was added with a micro-syringe. The capsule was then surrounded by components of
240 the solid media pressure cell (**Figure 1**), loaded into a pressure vessel with a $3/4$ " tungsten-carbide
241 core, and then end-loaded. The Ag capsule was pressure-sealed to a 2 mm thick Ag lid by
242 applying pressure to the sample piston with a hand pump.

243 Experiments were heated to 900, 800, or 725 °C with a ramp rate of ~300° per minute.
244 Specifically, they were ramped at 300 °C per minute to 25° below the set point, and then at 100°
245 per minute for the final 25°. The temperature was monitored using calibrated 25% WRe–3% WRe
246 thermocouple wire. The temperature choices result in approximately equivalent spacings when T
247 (in K) is expressed as $10^6/T^2$. The pressure was kept fixed at 1.5 GPa using a 20 cm Heise gauge
248 and experiment durations were 48, ~94, or 140 h for 900, 800, and 725 °C experiments,
249 respectively. Experiments were quenched by cutting power to the transformer. Prior to opening
250 the capsules, they were gently cleaned with a file and a lathe to remove Mg-oxide pressure media
251 and a small amount of the exterior wall the Ag capsule. All capsules exhibited evidence for
252 fluid-under-pressure, and expelled liquid once the water-tight seal was breached. In preparation
253 for MC-ICP-MS measurements, quartz crystals (50 – 300 μm) were extracted from the capsules
254 with tweezers, sonicated in ethanol, and then inspected for inclusions by reflected light,
255 transmitted light, and backscattered electron imaging. Zircon crystal picking was prohibitive due
256 to size ($\sim < 5$ μm), so aliquots were treated in dilute HF acid overnight to remove residual silica
257 quench or quartz. Hydrofluoric acid cleaning of non-metamict zircon effectively separates

258 zircon from other silicate material (e.g., Watson et al. 2006; Trail et al. 2009) and zircon crystal
259 surfaces are not altered by acid treatment (Cherniak and Watson, 2010).

260 To prevent entry of foreign material, HF treatment was carried out in a teflon container
261 that was loosely-capped, but the cap was not tightened based on the expectation that volatile
262 SiF₄, formed by reaction of the acid with quartz+quench, would be preferentially lost. After
263 treatment, the HF was carefully poured out of the container and discarded, with the last drop
264 wicked away with a kimwipe®. The remaining material was rinsed several times in ethanol and
265 dried. A small amount of pre- and post-treated “zircon fraction” was cast into epoxy, polished
266 with an automated polisher with a slurry of 1 μm Al₂O₃+H₂O, and then finished with colloidal
267 silica. Cathodoluminescence (CL) and secondary electron (SE) images were collected for the
268 samples.

269 2.1.2 Three-isotope exchange method

270
271
272 Our second set of experiments implemented the three-isotope exchange method (e.g.
273 Matsuhisa et al., 1978; Shahar et al., 2008), though were otherwise identical to the design
274 presented in Figure 1. The method involves doping one of the equilibrating phases – quartz in
275 this case – in the denominator isotope (²⁸Si). Quartz will thus plot below the terrestrial mass
276 isotope fractionation line (TMFL). The bulk composition of the quartz and undoped zircon
277 mixture will define a secondary mass fractionation line (SMFL; **Figure 2**). As these two phases
278 are brought to equilibrium by recrystallization at high temperature, each will progressively
279 approach the SMFL. The loci of the SMFL in isotope space is therefore constrained by the slope
280 of the SMFL and the isotopic composition of the system (i.e., quartz+zircon). Here we assume a
281 slope (γ) of 0.5178 for the SMFL based on equilibrium isotope fractionation theory:
282

$$283 \quad \gamma = \frac{\frac{1}{m_{29}} - \frac{1}{m_{28}}}{\frac{1}{m_{30}} - \frac{1}{m_{28}}} \quad (3)$$

284
285 where m_{28} is the mass of ²⁸Si, etcetera (Young et al., 2002). A series of isothermal experiments
286 conducted for progressively longer durations should produce an array of points for each phase
287 that trends toward the equilibrium fractionation value, defined by the intercept with the SMFL.

288 We prepared SiO₂ for our experiments by mixing reagent-grade SiO₂ with ²⁸Si-enriched
289 SiO₂ from Isoflex USA ®, with a stated purity of 99.4% ²⁸SiO₂. First, an initial mixture
290 containing about 1.1 wt% of isotopically-labeled SiO₂ was mixed with the same Alfa Aesar
291 material as the previous section. This was ground in a ceramic Al₂O₃-based mortar and pestle
292 (Diamonite ®) for approximately 1 hour. A small chip of the Diamonite® mortar was removed,
293 mounted in epoxy, polished, and analyzed by energy dispersive spectroscopy confirming that it
294 is Al₂O₃-based, with a binding agent containing Ca, Mg, Si, and Cr.

295 The ²⁸Si-enriched mixture yielded δ²⁹Si_{NBS-28} and δ³⁰Si_{NBS-28} values of ~-10.7 ‰. In
296 these experiments, it is important not to “overspike” with ²⁸SiO₂, so that the amount of
297 extrapolation to the SMFL is reasonable (Shahar et al., 2017). “Underspiking” may result in
298 changes to the equilibrating phases during the experiment that are too small to detect with the
299 MC-ICP-MS precision. Early attempts to conduct experiments with the above spiked mixture
300 were unsuccessful because the extrapolation to the SMFL was too large. Thus, we produced a
301 second SiO₂ mixture in which the δ³⁰Si ~-10.7 ‰ material was diluted further by adding
302 additional Alfa Aesar SiO₂ (TMFL) material. This resulted in a mixture consisting of about 0.29

303 wt% of isotopically-labelled $^{28}\text{SiO}_2$. Approximately 2 grams of SiO_2 was thoroughly mixed in a
304 Diamonite ® mortar and pestle for approximately 1 hour.

305 The zircon starting material was a ~5 gram crystal from the Mud Tank carbonatite
306 (Currie et al., 1992). The crystal was inspected optically and was found to be free of visible
307 inclusions, though it did contain infrequent and small (1-5 μm) secondary opaques, likely Fe-
308 oxides, along fractures in the crystal. It was crushed and ground under ethanol for approximately
309 1 hour. The resulting material was sieved to a size fraction smaller than 70 μm , and then ground
310 again. As later verified by SEM, this produced angular fragments of zircon which were expected
311 to have relatively high reactivity during the experiments. That is, the surfaces of crystal shards
312 are likely to have lower activation energy barriers causing them to more rapidly undergo
313 dissolution – and thus recrystallization – than primary crystal facets.

314 Silver capsules, of the same design described above, were loaded with equimolar
315 amounts of Si for each phase, resulting in a total weight of approximately 130 mg for each
316 experiment. For experiments performed at 900 and 800 °C, we added 4 wt. % of the same 10
317 mM CaCl_2 fluid to the capsule, which also contained trace DyCl_3 . Like the direct synthesis
318 experiments, the CaCl_2 was added because it has been shown to enhance re/crystallization of
319 zircon (e.g., Geisler et al. 2001). Based on the expectation that higher fluid contents would result
320 in faster equilibration, we added additional fluid (8 wt. % total) to our lowest temperature series
321 (725 °C). Dysprosium was included because it is a known cathodoluminescence emitter in
322 zircon and was thus used to evaluate the extent of recrystallization in trace element poor Mud
323 Tank zircon in the experimental products. Time series experiments ranged from 20 to 150 h for
324 900 °C, from 20 to 500 h for 800 °C, and from 20 to 1099 h for 725°C. At least 15 mg and 45
325 mg of cleaned quartz and zircon, respectively, were recovered from each experiment and
326 processed as for the direct synthesis experiments for MC-ICP-MS measurements.

327

328 **2.2 MC-ICP-MS measurement**

329

330 Starting materials, experimental products, and external standards were processed through
331 the same HF-free dissolution and purification procedure before Si isotope analysis. This method
332 is based closely on that described in detail in Georg et al. (2006) with specific modifications and
333 further details noted in Savage and Moynier (2013). The use of HF for sample dissolution is
334 avoided with use of an alkali flux digestion method. Each sample was weighed into a silver
335 crucible (made of 99.99% pure Ag sheet) along with enough NaOH flux (semiconductor grade,
336 99.99% pure, Sigma Aldrich) such that the mass ratio of sample to flux was ~1:20. The crucible
337 was then placed in a muffle furnace, heated to 720°C, for approximately 15 minutes. The
338 crucible was removed from the furnace, left to cool for 30 seconds, and submerged in ~ 20ml of
339 Milli-Q ® water (18.2 M Ω ·cm) in a PTFE container. The resultant fusion cake is water-soluble
340 and is readily removable from the crucible: this was performed by submitting the crucible-
341 containing PTFE container to ultrasonication and gentle heating, then pipetting the dissolved
342 cake into a pre-cleaned polypropylene bottle. The transferred fusion material is diluted further
343 with Milli-Q ® water and then acidified to 1% HNO_3 v/v with thermally distilled nitric acid
344 (~15.7 M) – the amount of HNO_3 added is calculated based on the mass of NaOH used in each
345 fusion. The degree of dilution (i.e., how much water is added to the final solution) is estimated,
346 based on the initial amount of sample dissolved, to allow for a final solution concentration of
347 between 10 and 20 ppm Si. The Si concentration in each solution is determined photometrically
348 using the “Heteropoly-Blue” method (with Hach-Lange ® Ultra-low range Si reagents) and

349 fusion yield estimated based on the weighed amount of sample and the measured ppm of Si. The
350 calculated fusion yields were all between 95 and 99% Si recovery.

351 The Si from the samples and standards were purified using a one-step column procedure
352 utilizing 1.8ml of BioRad AG50 X-12 (200-400 mesh) cation exchange resin loaded into BioRad
353 “Poly-Prep” columns, again following methods detailed in Georg et al. (2006) and Savage and
354 Moynier (2013). Silicon in neutral to acidic media does not adhere to the resin, and elutes
355 straight through, whereas other cations are held on to the resin and are quantitatively removed
356 from the matrix. All other anions, if present, are at too low concentrations relative to Si to affect
357 isotopic measurement (c.f. Georg et al 2006). Total procedural blanks are on the order of 0.1 μg
358 Si, which typically represents $\sim 0.35\%$ of total Si and are therefore negligible.

359 Over the course of this study, Si isotope measurements were made on two Neptune Plus
360 Multi-Collector Inductively Coupled Plasma Mass spectrometers (MC-ICP-MS); one at the
361 Institut de Physique du Globe de Paris (IPGP), the second in the St Andrews Isotope
362 Geochemistry (STAiG) laboratories. Running conditions for both instruments are as described in
363 Trail et al. (2018) and more general details are provided in Savage and Moynier (2013). Both
364 instruments were operated in ‘medium’ resolution mode to avoid polyatomic interferences (in
365 particular the large $^{14}\text{N}^{16}\text{O}^+$ interference that would otherwise overwhelm the $^{30}\text{Si}^+$ signal).
366 Samples were introduced to the instrument using a $75 \mu\text{l min}^{-1}$ ESI PFA microflow nebulizer via
367 the Thermo Scientific “SIS” spray chamber.

368 Samples were analyzed at a concentration of 2 ppm Si, which gave $\sim 16\text{V}$ on the ^{28}Si
369 beam (using a $10^{11} \Omega$ resistor) in medium resolution mode. Ratios were measured in static mode,
370 and each measurement consisted of 25 cycles of ~ 3 s integrations with a 3 s idle time. Sample
371 $\delta^{29}\text{Si}$ (i.e., $[(^{29}\text{Si}/^{28}\text{Si})_{\text{sample}}]/(^{29}\text{Si}/^{28}\text{Si})_{\text{NBS-28}} - 1] \times 1000$) and $\delta^{30}\text{Si}$ values were calculated using the
372 standard-sample bracketing method (relative to NIST RM 8546 silica sand, historically called
373 NBS-28). Aliquots of the USGS geostandard BHVO-2 and the Si standard ‘Diatomite’ were
374 routinely ran alongside the unknown samples to monitor accuracy. These analyses are given in
375 Table 1. Our analyses match the ‘accepted’ reference values for these standards exactly
376 (Reynolds et al., 2007; Savage et al., 2014). Standards “BHVO-2 STAiG old” and “Diatomite
377 STAiG” are aliquots taken from the same sample dissolutions as those for the relevant IPGP
378 measurements; comparison of these data show that there is no systematic instrumental offset
379 between the two measurement locations. Additionally, “BHVO-2 STAiG new” is a repeat
380 dissolution of BHVO-2 performed at St Andrews; the lack of offset between this datum and
381 previous BHVO-2 measurements shows that Si isotope analysis at St Andrews produces accurate
382 data with comparable precision.

383

384 **3 Results**

385

386 **3.1 Images and description of experimental products**

387

388 Electron microscopy shows that the zircon crystals produced by direct synthesis are
389 relatively euhedral and approximately 1 to 5 μm (**Figure 3a**). Quartz crystals from the same
390 experiments (not shown) were approximately 50 to 300 μm . With respect to the three-isotope
391 exchange method, the crushed Mud Tank zircon shards used in experiments show clear evidence
392 for recrystallization, analogous to observations made by Ayers et al. (2018) for their zircon-fluid
393 partitioning experiments. An example secondary electron image of the starting material reveals

394 numerous angular fragments (Fig. 3b) that exhibit evidence for dissolution as the experiment
395 duration is increased (Fig. 3c,d).

396 “Zircon fractions”, extracted directly from the capsule after hand cleaning, showed
397 occasional quartz (Fig. 3c). After treatment of this material in cold HF acid, no evidence for
398 quartz remained. In post-treated zircon fractions, we did not see evidence for quenched SiO₂ in
399 epoxy grain mount either. If HF treatment removes the quartz, it is reasonable to expect that the
400 quench material, with smaller size (<<50 μm) and larger surface area to volume ratios, are also
401 likely removed. These results, including the observations made after the HF cleaning procedure,
402 agree with past studies (Trail et al., 2009). Quartz crystals are mostly free of inclusions, though
403 they do contain rare occurrences of sub- to micron-sized zircons (Fig. 3e). We estimate that all
404 mineral aliquots separated for isotope analyses were >95% pure.

405 Evidence for zircon recrystallization is also present through inspection of CL images.
406 While the starting material shows only modest luminescence (Fig. 3f), the experimental products
407 show evidence of recrystallization near the rims of the crystals (Fig. 3g-i). This is caused by
408 substitution of CL-active Dy, added as a trace impurity in the starting fluid, into the zircon
409 lattice.

410

411 3.2 Silicon isotope data

412

413 Silicon isotope ratios (³⁰Si/²⁸Si and ²⁹Si/²⁸Si) are reported relative to NBS-28 quartz sand.
414 Table 1 provides external standard data, and Tables 2 and 3 contains the analyses of the direct
415 synthesis and 3-isotope experimental run products, respectively. Analytical errors for individual
416 phases represent the 2 standard deviations (2 s.d.) of 4 to 5 analyses of a purified sample aliquot
417 (Tables 2 and 3).

418 The long-term external reproducibility of the MC-ICP-MS measurements can be assessed
419 using external standard data; each Si isotope analytical session includes measurement of an
420 aliquot of BHVO-2 (and often Diatomite) which was processed through chemistry at the same
421 time as the other samples being analyzed. The long-term reproducibility can be therefore
422 quantified by calculating the 2 × standard deviation of the δ³⁰Si_{NBS-28} and δ²⁹Si_{NBS-28} BHVO-2
423 (and Diatomite) values generated in each measurement session. As each standard measurement
424 also represents a separate chemical separation procedure, this reproducibility also takes into
425 account the variations in the Si isotope separation method. For the IPGP instrument, over a
426 period of 5 months, the external precision on BHVO-2 was δ³⁰Si_{NBS-28} ± 0.04‰ and δ²⁹Si_{NBS-28} ±
427 0.03‰ (2 s.d.). For the St Andrews instrument, over a period of 9 months, the external precision
428 on both BHVO-2 and Diatomite was δ³⁰Si_{NBS-28} ± 0.03‰ and δ²⁹Si_{NBS-28} ± 0.03‰ (2 s.d.).

429 These long term external reproducibilities are comparable to, and are mostly lower than,
430 the 2 s.d. values calculated for each individual sample measurement, based on the 4 or 5 analyses
431 of the same purified sample aliquot (Tables 2 and 3). For simplicity, we could choose to apply
432 the external precision to all data. However, this does not tell the whole story, as instrumental
433 running conditions can be variable, and will differ between each measurement session, meaning
434 that “short-term” precision on sample measurements will also differ. Because samples are often
435 measured only once, and all samples presented in this study were not measured during the same
436 session, we prefer to utilize the individual analytical errors (as 2 s.d.) in the subsequent
437 discussion and error propagation.

438

439 3.2.1 Direct synthesis

440
441
442
443
444
445
446
447

Direct synthesis experiments yield $\Delta^{30}\text{Si}(\text{qtz-zrc})$ values of 0.27 ± 0.07 , 0.29 ± 0.09 and 0.21 ± 0.08 ‰ for respective temperatures of 725, 800, and 900 °C (Table 2). The $\Delta^{30}\text{Si}(\text{qtz-zrc})$ errors are calculated via $(\sqrt{[(\text{err}_{\text{qtz}})^2 + (\text{err}_{\text{zrc}})^2]})$, using 2 s.d. errors for quartz and zircon. The measured $\delta^{30}\text{Si}_{\text{NBS-28}}$ value of the starting material is -0.14 ± 0.05 ‰. In all three cases, this is less than 0.1 ‰ from calculated mass balance values of the experiments. Considering the average error associated with this estimate (± 0.08 ‰), the average Si isotopic composition for quartz and zircon supports Si isotope mass balance for the direct synthesis experiments.

448 *3.2.2 Three-isotope method.*

449

450 The $\delta^{29}\text{Si}$ and $\delta^{30}\text{Si}$ values for starting materials and experimental products are reported
451 in Table 3. The starting material for 900 and 800 °C experiments consisted of quartz pre-
452 synthesized in a piston cylinder device, whereas the starting material for the 725 °C experiments
453 used mechanically mixed SiO_2 powder without pre-synthesis. The $\delta^{30}\text{Si}(\text{ave})$ column is
454 calculated by taking the average $\delta^{30}\text{Si}(\text{qtz})$ and $\delta^{30}\text{Si}(\text{zrc})$ for each experiment, and assuming a
455 1:1 quartz to zircon ratio, by mole. This reveals that the experimental charges exhibit very good
456 agreement with the average isotopic composition of the starting material, which indicates the
457 experiments approximate a closed system with respect to Si (**Figure 4**). When compared to the
458 starting materials, Si isotopic compositions of quartz and zircon show progressive exchange for
459 longer experiment durations. A simple percent exchanged calculation, which compares the
460 amount of isotope exchange between the initial and the experimental product with the difference
461 between the initial composition and intercept, ranges between 15 and 36%.

462 After Figure 2, the starting compositions and the measured phases for each isotope
463 exchange experiment were plotted on a $\delta^{29}\text{Si}$ vs. $\delta^{30}\text{Si}$ plot. A line was fitted to the data using a
464 York regression in the Origin 2016 ® software package. This line was extrapolated to intercept
465 the SMFL. In all cases, our three sets of experiments show quartz and zircon approaching the
466 SMFL. Intercepts and the errors were solved for each zircon and quartz pair. These intercepts
467 constrain the $\Delta^{30}\text{Si}(\text{qtz-zrc})$ at each of the three experiment temperatures.

468 These intercepts are also constrained by mass balance of the system (Figure 4). To take
469 this into consideration, our final calculated fractionations involved a Monte Carlo simulation of
470 possible $\Delta^{30}\text{Si}(\text{qtz-zrc})$ equilibrium values constrained by the SMFL intercept, the 95%
471 confidence intervals associated with the SMFL intercept, and the mass balance of the system.
472 Inputs for $\delta^{30}\text{Si}(\text{qtz})$ and $\delta^{30}\text{Si}(\text{zrc})$ were randomly generated by assuming the probability of
473 distribution was defined by the 95% confidence intervals of the intersection to the SMFL. The
474 next criterion requires that selected $\delta^{30}\text{Si}(\text{qtz})$ and $\delta^{30}\text{Si}(\text{zrc})$ values satisfy mass balance of the
475 system, where tolerances for this criterion are provided on Figure 4. We randomly selected
476 10,000 $\delta^{30}\text{Si}(\text{qtz})$ and $\delta^{30}\text{Si}(\text{zrc})$ SMFL intercept values that satisfy mass balance, and the
477 average of these results was used to predict the fractionation. In general, the errors associated
478 with the York fits for zircon were smaller and quartz. While the error on the fit may be larger if
479 quartz is considered independently, the error becomes smaller when the mass balance constraint
480 is utilized. The standard deviation of the successful Monte Carlo sampling was used to calculate
481 the error (see the Electronic Annex for additional details). Our calculated $\Delta^{30}\text{Si}(\text{qtz-zrc})$
482 fractionations for 900, 800, and 725 °C are 0.40 ± 0.46 , 0.51 ± 0.18 , and 0.50 ± 0.29 ‰ (2 s.d.),
483 respectively (**Figure 5**).

484

485 **4 Discussion**

486

487 **4.1 Si isotope quartz-zircon fractionation calibration**

488

489 For each experiment, the orthosilicate zircon preferentially incorporates the lighter
490 isotopes of Si relative to quartz, as predicted by first principles equilibrium isotope theory and
491 previous – but limited – natural sample measurements (Méheut et al., 2009; Savage et al., 2012;
492 Qin et al., 2016; Trail et al., 2018). However, there is systematic shift between the fractionation
493 factors determined via the direct synthesis and three-isotope exchange methods. The average
494 difference between the larger $\Delta^{30}\text{Si}(\text{qtz-zrc})$ fractionations calculated for the three-isotope
495 exchange method, compared to the direct synthesis experiments for the three temperatures, is
496 0.18 ‰. This difference is smaller than the average $\Delta^{30}\text{Si}(\text{qtz-zrc})$ three-isotope method errors
497 (± 0.31 ‰, 2 s.d.). The error calculated for the direct synthesis is 0.08 ‰ (2 s.d.), which only
498 takes into consideration the reproducibility of the measurements. The larger errors associated
499 with the three-isotope method are because they represent the uncertainty of the measurements
500 *and* the extrapolation of phases – that exchanged at most ~40% of their Si during the experiment
501 – to the SMFL. Although the direct synthesis and three-isotope methods yield $\Delta^{30}\text{Si}(\text{qtz-zrc})$
502 values that are similar when error is considered, this sort of magnitude in Si isotope space is on
503 the same order as the isotopic difference between basaltic and rhyolitic magmas (Savage et al.,
504 2011), and is therefore worth commenting upon. Here we explore potential reasons that may be
505 affecting the resultant isotope fractionations predicted using both methods.

506 First, there are limited experimental studies in which Si isotope fractionations between
507 phases have been characterized by different techniques for comparison. There are, however,
508 experimental data for Si isotope fractionations between molten silicate and metal, which used
509 methods similar to the direct synthesis and three-isotope methods employed here (Shahar et al.
510 2009; 2011; Hin et al. 2014). While silicate-metal systems are not directly analogous to our
511 experiments, they are of interest here because the different techniques utilized in these studies
512 yielded different $\Delta^{30}\text{Si}(\text{silicate-metal})$ vs. $1/T^2$ calibrations. For experiments conducted using the
513 three-isotope scheme, the silicate material was doped with ^{28}Si to trace the exchange of Si
514 between the metal and silicate. Experiments were performed at 1 GPa or 7 GPa, and from 1800
515 to 2200 °C (Shahar et al., 2009; 2011). On the other hand, Hin et al. (2014) experimentally
516 calibrated the Si isotope fractionation between metal and silicate liquids using undoped
517 materials, though with other deviations from the general design of Shahar et al. (2009; 2011).
518 For instance, Hin et al. (2014) used modest to moderately different starting compositions. The
519 main differences were that they added a combined total of ~2.5 wt% Na_2O and K_2O to their
520 silicate mixture, and used a Fe-Si metal which contained ~1 wt% Mo and 10 wt% Sn for most of
521 the experiments. That said, the absence of Sn from two of their experiments did not lead to an
522 appreciable change in their $\Delta^{30}\text{Si}(\text{silicate-metal})$ vs. $1/T^2$ relationship. Hin et al. (2014) also used
523 a centrifuging piston cylinder for most of their experiments, though for a single experiment
524 conducted in a standard piston cylinder, the $\Delta^{30}\text{Si}(\text{silicate-metal})$ vs. $1/T^2$ relationship was not
525 appreciably different. With these differences and comparisons noted, Hin et al. (2014) reported
526 smaller $\Delta^{30}\text{Si}(\text{silicate-metal})$ fractionations than those of Shahar et al. (2011), once temperature
527 is considered. As a specific example, Hin et al. (2014) predicts $\Delta^{30}\text{Si}(\text{silicate-metal}) = -$
528 1.08 ± 0.01 ‰ at 1750 °C, whereas the three-isotope calibration of Shahar et al. (2011) yields
529 $\Delta^{30}\text{Si}(\text{silicate-metal}) = -1.82 \pm 0.10$ ‰ at the same temperature. The explanation for this
530 difference suggested by Hin et al. (2014) is that some Si was lost to the capsule thus
531 compromising the simple application of the three-isotope method presented in Figure 2. In our

532 experiments, we can rule out loss of Si to the capsule wall as Si-oxide is insoluble in Ag. The
533 fluid medium does result in dissolved silica during the experiment, which leads to a loss of silica
534 from the SiO₂-zircon system. This effect appears to be negligible as it pertains to the isotopic
535 composition of the system, an inference based on the attainment of isotope mass balance for each
536 experiment (i.e. Figure 4). Hence, this is unlikely to be the explanation for the systematic offsets.

537 A second possibility is that, in the isotope exchange setup implemented here, the degree
538 of reaction of one of the starting materials with the fluid component could have been larger than
539 for the other phase. The direct synthesis method does not require dissolution of pre-existing
540 zircon which can be temporally prohibitive due to the refractory nature and slow dissolution
541 kinetics of zircon. This would essentially mean that calculation of the SMFL based on an
542 equimolar mixture is incorrect. However, this effect does not seem to be pronounced in our
543 experiments because the average composition of the experimental products agree with the
544 starting composition, and the calculated percent exchanged for zircon and quartz pairs in
545 individual experiments are in broad agreement (**Figure 6**).

546 A third possibility – fractionation of isotopes by diffusion – is not considered a viable
547 explanation for the differences observed either. While such effects may be possible in
548 experiments in which metal is a phase of interest (Lazar et al., 2012), the diffusion of cations in
549 most mineral oxides are not fast enough in most scenarios. The images presented in Figure 3
550 show that recrystallization during the experiments occurs at the micron-scale for zircon. The
551 scale is perhaps tens of microns for quartz if the zircon inclusions identified within the quartz
552 crystals are used as a marker (Figure 3e). These distances are significantly longer than length
553 scales for self-diffusion of Si in quartz and zircon. The characteristic diffusive length scale
554 ($[4D \cdot t]^{1/2}$, D = diffusivity and t = time) for Si in quartz is only ~1 nm for a temperature of 900 °C
555 and a duration of 10⁴ years using the Arrhenius relationship of Bějina and Jaoul (1996). The
556 same temperature and time yield a similar length scale for self-diffusion of Si in zircon
557 (Cherniak, 2008). While these calculations were conducted by extrapolating diffusivities
558 collected from ~1600 to 1300 °C down to 900 °C, the resulting characteristic diffusive length
559 scales strongly suggest kinetic effects related to self-diffusion of Si are not important, when
560 compared to recrystallization. The slow diffusivities of Si in quartz and zircon also mean that
561 time series experiments are not likely to fully remove any kinetic-based isotope fractionations
562 due to crystal growth.

563 A fourth possibility to consider is the crystallization of the phases of interest during
564 heating of the direct synthesis experiments. Non-equilibrium fractionations were invoked by
565 Clayton et al. (1972) to explain the discrepancy between quartz-fluid oxygen isotope
566 fractionation synthesis and exchange experiments whose heating times range between 20 and 40
567 minutes for temperatures of 250 to 500 °C. No evidence for disequilibrium was reported for
568 experiments conducted at 750 °C for experiments of a similar design (Clayton et al., 1972). Our
569 experiments were heated at a rate of ~300°/min, to lessen the severity of this effect, however we
570 return to the issue of early phase nucleation in light of the differences in isotope fractionations
571 measured between the two techniques. To supplement our understanding of the heating step, we
572 conducted a ‘zero time’ experiment. This was heated at 300°/min to 900 °C and then
573 immediately quenched. All other aspects of the experiment were identical to the direct synthesis
574 procedure presented in section 2.1.1. The heat-treated product was extracted from the capsule,
575 and an X-ray diffraction (XRD) pattern was collected with no other sample preparation. For
576 comparison, an XRD pattern was also collected for the starting material. This revealed a starting
577 material that is almost exclusively amorphous – with a minor fraction of tridymite detected –

578 whereas the heat-treated product contains evidence for abundant quartz and zircon (Electronic
579 Annex). Element transport of O during the heating process is unlikely to be restricted, that of Si
580 is likely is highly restricted, with crystallization occurring without full chemical communication
581 of the entire capsule. While speculative, this scenario may result in an underestimate of Si
582 isotope fractionation factor, with both phases having compositions closer to the bulk
583 experimental composition.

584 The presence of nucleated zircon and quartz during heating, coupled with the low
585 expected transport of silica, is reason to consider the direct synthesis fractionations with caution.
586 We therefore consider the fractionations derived from the three-isotope method experiments to
587 be the best reflection of equilibrium fractionations. These $\Delta^{30}\text{Si}(\text{qtz-zrc})$ data are plotted
588 against $1/T^2$ (in K) and fitted by regressing through the origin. This latter constraint is common
589 among stable isotope fractionation studies, whether used for theoretical results, experimental
590 data, or empirical studies (e.g. Qin et al., 2016; Shahar et al. 2009; Valley et al., 2003), which
591 significantly reduces the error on the slope in almost all cases. We assume that this constraint is
592 applicable here for our data, and in doing so, an A -value of 0.53 ± 0.14 is obtained using only the
593 three-isotope fractionations (equation 2).

594

595 **4.2 Comparison of Si isotope quartz-zircon fractionations**

596

597 While we view this A -value estimation as capturing the pertinent features of our data, this
598 it is not as robust as A -values reported for other isotope systems (e.g., Shahar et al., 2008), due to
599 the slower approach to equilibrium of silicate phases. We use this section to provide a simple
600 comparison of other available constraints and predicted $\Delta^{30}\text{Si}(\text{qtz-zrc})$ fractionations. The latter
601 are provided at 700 °C, a typical temperature for zircon crystallization in terrestrial magmas (e.g.,
602 Watson and Harrison, 1983; Watson et al., 2006; Boehnke et al., 2013). Using an A -value of
603 0.53 presented in the previous section yields a $\delta^{30}\text{Si}(\text{qtz})$ value 0.56 ‰ higher than co-existing
604 zircon at 700 °C. If only data from the direct synthesis experiments are used, this would yield
605 $\Delta^{30}\text{Si}(\text{qtz-zrc}) = 0.32\text{‰}$. Trail et al. (2018) reported Si isotope measurements for an aliquot of
606 zircon ($\sim 10^3$ grains) and quartz from the Lachlan Fold Belt Jindabyne tonalite. The zircons from
607 this tonalite have an average crystallization temperature of 755 °C (Trail et al., 2017). Assuming
608 this temperature represents crystallization T of the mineral pair, and that $\Delta^{30}\text{Si}(\text{qtz-zrc})$ tends
609 toward zero when temperature tends toward infinity, an A -value of 0.50 can be calculated (and a
610 $\Delta^{30}\text{Si}(\text{qtz-zrc}) = 0.53 \text{‰}$ at 700 °C). While the direction of the predicted fraction is the same for
611 both experimental methods, these natural data are in best agreement with the A -value calculated
612 with three-isotope method experiments. Finally, Qin et al. (2016) reported calculations, based on
613 density functional theory, to quantify the fractionation factors for a wide range of silicates. This
614 study predicts a $\Delta^{30}\text{Si}(\text{qtz-zrc})$ fractionation of 0.39 ‰ at 700 °C, which is in closest agreement
615 with the direct synthesis only work presented here. A summary of these fractionations is
616 provided in **Figure 8** and Table 4.

617

618 **4.3 Inferring whole rock Si isotope composition from out-of-context zircon and quartz**

619

620 A goal of this work is to better constrain the Si isotope composition of an igneous rock
621 via analysis of zircon or quartz, as both minerals are common in the detrital record. Here, we
622 provide a relatively robust parametrization to allow for this, albeit within a simplified model. The
623 first requirement is to explore how the $\delta^{30}\text{Si}(\text{qtz})$ and $\delta^{30}\text{Si}(\text{zrc})$ values relate to the whole rock

624 (WR). In general, the present observations of natural samples show that the quartz Si isotope
625 composition is a broad proxy for WR $\delta^{30}\text{Si}$. Felsic WR and mineral separate data reported by
626 Savage et al. (2012) show that quartz is generally isotopically heavier than whole rock, but with
627 only a small (+0.05‰) enrichment in the heavier Si isotopes. This is perhaps not surprising,
628 especially in granites, where quartz has high modal abundances. For example, for a $\delta^{30}\text{Si}_{\text{NBS-28}}$
629 $_{28}(\text{zrc}) = -0.55$ ‰, we predict a $\delta^{30}\text{Si}_{\text{NBS-28}}(\text{qtz})$ of -0.05 ‰, for a crystallization temperature of
630 ~ 700 °C. This would give an approximate $\delta^{30}\text{Si}_{\text{NBS-28}}(\text{WR})$ of -0.10 ‰.

631 However, the nature of the $\Delta^{30}\text{Si}(\text{WR-zrc})$ relationship is less predictable as host-rock
632 composition (and mineralogy) change. In other words, there is no simple isotope relationship
633 between the WR and mineral because this relationship is a function of WR mineralogy and
634 composition. Nevertheless, broad predictions can be made within our current framework of
635 understanding. As mentioned, it appears that the relative polymerization degrees of the various
636 mineral and melt phases exert a strong control on the relative Si isotope fractionation between
637 these phases. High- SiO_2 melts are both highly polymerized and typically precipitate framework
638 silicates such as quartz, feldspars, and feldspathoids which tend to prefer the heavier isotopes of
639 Si. Zircon (an orthosilicate) crystallizing in this system should therefore strongly favor the
640 lighter isotopes of Si. The largest $\Delta^{30}\text{Si}(\text{WR-zrc})$ should therefore be associated with zircons
641 formed from high- SiO_2 melts, because these systems also crystallize at the lowest temperatures.
642 It is also likely that in evolved but silica-undersaturated systems, where feldspathoids dominate,
643 the difference in polymerization degree between these minerals and zircon – if saturated – should
644 still mean that our $\Delta^{30}\text{Si}(\text{qtz-zrc})$ calibration will provide a broad estimate of whole-rock Si
645 isotope composition.

646 It is less clear how $\Delta^{30}\text{Si}(\text{WR-zrc})$ will scale with significantly lower bulk SiO_2
647 concentration, but we predict that this magnitude will be smaller for zircons crystallizing from
648 more primitive melts. This could be particularly important for kimberlitic zircons; although their
649 petrogenesis is debated, they are often found intergrown with mafic phases such as Fe-rich
650 olivine, Cr-rich diopsides, and Fe-Ti oxides (Spetsius et al., 2002; Page et al., 2007). The
651 difference in polymerization degree between these phases is minimal, and hence this factor
652 should not exert such a strong control on the Si isotope composition of zircons in this system.

653 In fact, (limited) measurements and calculations do imply that $\Delta^{30}\text{Si}(\text{WR-zrc})$ positively
654 correlates with the SiO_2 content of the WR (Qin et al. 2016; Trail et al., 2018). For instance,
655 Trail et al. (2018) reported a $\Delta^{30}\text{Si}(\text{WR-zircon})$ value of 0.37 ‰ for a tonalite (~ 65 wt% SiO_2),
656 which broadly agrees with calculations by Qin et al. (2016) who estimated a $\Delta^{30}\text{Si}(\text{WR-zrc})$
657 fractionation for an intermediate felsic rock of ~ 0.3 ‰ at 750 °C. Moreover, the Duluth Gabbro
658 “mantle” zircons analyzed by Trail et al. (2018) have $\delta^{30}\text{Si}_{\text{NBS-28}} \approx -0.36$ ‰, which is only subtly
659 lighter than the current estimate for bulk silicate Earth (-0.29 ± 0.07 ‰, Savage et al., 2014). The
660 effect that decreasing the SiO_2 content of the system is predicted to have on $\Delta^{30}\text{Si}(\text{WR-zrc})$ is
661 illustrated in **Figure 9**, where the “mafic” value for A (see equation 2) is estimated from the
662 offset of Duluth Gabbro zircons from Si isotope composition of the mantle ($\delta^{30}\text{Si}(\text{BSE}) = -0.29$
663 ‰; Savage et al., 2014) and a formation temperature of 800 °C. It is shown schematically that
664 $\Delta^{30}\text{Si}(\text{WR-zrc})$ should decrease as SiO_2 of the system decreases; however it should not be
665 assumed that $\Delta^{30}\text{Si}(\text{WR-zrc})$ and SiO_2 content will vary linearly. This schematic predicts that,
666 when estimating $\delta^{30}\text{Si}(\text{WR})$ from an out-of-context zircon, one might over- or underestimate the
667 whole rock composition by around 0.25 ‰, which is on the order of the precision of a typical ion
668 microprobe Si isotope measurement.

669 Constraining the sensitivity of $\Delta^{30}\text{Si}(\text{WR-zrc})$ to whole-rock SiO_2 is potentially important
670 for better bulk-rock Si isotope composition from Archean-age and older zircons, where the bulk
671 composition of the continental crust is a subject of debate (e.g. Harrison et al., 2017; Greber et al.
672 2017; Caro et al., 2017; Cawood and Hawkesworth, 2019; Deng et al., 2019). Nevertheless,
673 zircons crystallizing from a melt derived from purely igneous sources – i.e., without the
674 involvement of “weathered” material – are expected to display a $\delta^{30}\text{Si}_{\text{NBS-28}}$ range from -0.70 to -
675 0.35‰ (if we base the higher bound on the Duluth Gabbro sample). This inference applies to
676 rocks with ~50-78 wt.%, SiO_2 . Deviations from this $\delta^{30}\text{Si}_{\text{NBS-28}}(\text{zircon})$ range should indicate the
677 presence of “non-igneous” material in the melt source.

678

679 4.4 $\Delta^{30}\text{Si}(\text{qtz-zrc})$ and $\Delta^{18}\text{O}(\text{qtz-zrc})$ as geothermometers?

680

681 Our experiments and natural measurements predict resolvable Si isotope inter-mineral
682 fractionations between zircon and quartz in igneous systems, larger than most other mineral-
683 mineral pairs (Savage et al., 2011, 2012; Trail et al., 2018). This opens the possibility that
684 $\Delta^{30}\text{Si}(\text{qtz-zrc})$ values could be used as a geothermometer in rocks where quartz and zircon are in
685 equilibrium. In this regard, a key source of comparison is the widely used Ti-in-zircon
686 geothermometer and the Ti-in-quartz geothermobarometer (Watson and Harrison, 2005; Ferry
687 and Watson, 2007; Thomas et al., 2010). This method requires measurement of the Ti content in
688 the phase-of-interest, which is a simple measurement by *in-situ* techniques. The calibrations are
689 precise ($\sim\pm 20$ °C) though there may be uncertainties in the titania activity during zircon and
690 quartz saturation, which could propagate additional uncertainties into the final calculated
691 temperature. Watson and Harrison (2005) estimate a *ca.* 50° increase in the calculated zircon
692 crystallization temperature for titania activities that change from 1 to 0.5. The titania activity
693 term does not simply cancel out if both phases are considered together because the Ti
694 concentration in quartz is pressure-dependent too (Thomas et al., 2010).

695 However, $\Delta^{30}\text{Si}(\text{qtz-zrc})$ or $\Delta^{18}\text{O}(\text{qtz-zrc})$ fractionations can only provide crude inferences
696 about the crystallization temperature, if reasonably pure aliquots of zircon and quartz are
697 obtainable. Such a measurement is also significantly more complex analytically. A measured
698 $\Delta^{30}\text{Si}(\text{qtz-zrc})$ of 0.56 ‰ with a precision of 0.06 ‰ would result in a temperature estimate of
699 $\sim 700\pm 150$ °C (2 s.d.). A similar calculation for $\Delta^{18}\text{O}(\text{qtz-zrc}) = 2.46$ ‰ with a precision of 0.2
700 ‰ yields $\sim 700\pm 130$ °C when the O isotope $A_{\text{qtz-zrc}}$ of 2.33 ± 0.24 is applied (Trail et al., 2009).
701 Thus, the current calibrations do not make useful geothermometers, given that errors are so large
702 as to make any such T-based calculation to be of limited value. Considering the isotope systems
703 together, however, may help evaluate whether the two phases crystallized in equilibrium (**Figure**
704 **10**). The slope of $\Delta^{18}\text{O}(\text{qtz-zrc})$ vs. $\Delta^{30}\text{Si}(\text{qtz-zrc})$ fractionation vs. T is 4.4, reflecting the ratio
705 of the A-values. Coupled measurements of Si and O isotopes in zircon and quartz that are well
706 resolved from a slope of 4.4 ± 1.5 (2 s.d) are likely to have crystallized out of equilibrium.

707 While these igneous T estimates are very crude by most modern techniques, there are
708 systems where such strategies could be of value. Recently, Ackerson et al. (2018) measured Ti
709 contents in quartz from the Tuolumne Intrusive Suite, located in the central Sierra Nevada,
710 California. Coupled with independent pressure estimates, the low Ti contents were interpreted to
711 reflect crystallization temperatures from ~475 to 560 °C. This was not predicted to be an isolated
712 occurrence; for instance, perhaps 75% of the quartz in this suite could have crystallized 100 to
713 200 °C below the wet granite solidus (Ackerson et al., 2018). The use of coupled $\Delta^{18}\text{O}(\text{qtz-zrc})$
714 and $\Delta^{30}\text{Si}(\text{qtz-zrc})$ to probe temperature is potentially appealing because the low predicted

715 temperatures will result in larger fractionations. In the case of the former, if the same precisions
716 for $\Delta^{18}\text{O}(\text{qtz-zrc})$ and $\Delta^{30}\text{Si}(\text{qtz-zrc})$ specified above are applied, the error on both temperature
717 estimates is ~ 100 °C (2 s.d.) at 500 °C, which may be sufficient to explore the low temperature
718 histories of granites or metamorphic systems in certain situations. At low temperatures, such
719 isotope fractionations may be advantageous over the well-established Ti-in-zircon thermometry
720 because the predicted Ti concentration in the presence of rutile and quartz is only ~ 0.2 ppm Ti at
721 500 °C, which makes this a more challenging measurement than typical igneous zircons.

722

723 5. Outlook

724

725 Since Si and O are abundant in the lithosphere and exhibit isotope fractionations at low
726 temperatures, it is logical to consider both systems when probing the nature of water rock
727 interactions and crustal weathering. This advantage, for example, was used to explore weathering
728 and precipitation processes in Archean greenstone belts. Abraham et al. (2011) measured bulk
729 rock $\delta^{30}\text{Si}$ and $\delta^{18}\text{O}$ values of silicified basalts and bedded cherts from the Barberton Greenstone
730 belt. This belt exhibits variable degrees of silica alteration, which is evidence for active silica
731 cycle, including mobilization and precipitation on the Archean Earth. Authigenic, seawater-
732 derived silica tends to have positive $\delta^{30}\text{Si}$ relative to igneous rocks because of the enrichment of
733 heavier isotopes in riverine silica, which is the major Si flux to the oceans (Frings et al., 2016).
734 This study discovered enrichments in ^{18}O and ^{30}Si correlated with increasing silicification,
735 implying that seawater was the dominant source of this silica.

736 Coupled Si-O isotope investigations have also been performed on the mineral scale, with
737 *in-situ* ion microprobe measurement of authigenic silica such as chert. In cases where chert or
738 quartz forms via hydrothermal precipitation, either in a marine or continental setting, the O and
739 Si isotope signatures in silica can reflect the degree of fractionation from hydrothermal fluids.
740 The trajectory and magnitude of $\delta^{18}\text{O}$ and $\delta^{30}\text{Si}$ in these silica precipitates is a strong function of
741 the hydrothermal environment and the fluid to rock ratio (Kleine et al., 2018), in addition to Si
742 isotope equilibrium fractionations (Pollington et al., 2016). Deviations in silica $\delta^{30}\text{Si}$ from
743 mantle values in Archean banded iron formations were interpreted to be the product of marine
744 hydrothermal activity, with a minor fraction of input from continental weathering (Heck et al.,
745 2011). Other possibilities include input from continent-derived freshwaters (~ 10 %) and very
746 minor (< 0.1 %) high-T hydrothermal activity (Delvigne et al., 2012).

747 While the geologic record is not always permissive of direct interrogation of sedimentary
748 material to trace low temperature surficial processes, burial and assimilation of this material into
749 crustal melts means that such chemical information may be inherited in igneous rocks. Whole
750 rock (WR) measurements are obvious targets, though in some cases, mineral-scale measurements
751 are the only possibility. With the goal of extracting useful and interpretable isotope information
752 from single minerals in igneous systems, high temperature (igneous) isotope fractionations must
753 be characterized. Our report of $\Delta^{30}\text{Si}(\text{qtz-zrc})$, to our knowledge, is the first experimental study
754 to characterize Si isotope fractionation between igneous silicate minerals. In this case, the
755 pertinent question bears not just on the isotopic composition of the mineral in question, but
756 whether this information can be used to provide clues about the composition of the melt from
757 which the mineral crystallized, and furthermore, about the material involved in the formation of
758 the melt (Trail et al., 2018). Our results enable, to first order, separation of contamination by low
759 temperature weathering products into magmas, and the subsequent high-temperature
760 fractionation that exists between silicate phases. These experimental data help establish Si

761 isotopes as an emerging geochemical tool that could be used in combination with O isotopes to
762 address key issues about the character and evolution of crust-atmosphere-hydrosphere
763 interactions that span the breadth of Earth history. Detrital quartz and zircon are two clear cases
764 where mineral-scale observations – and corresponding predictions about the composition of the
765 host rock – will be of value. The most obvious application to target is zircon because it can be
766 dated by U-Pb geochronology, though by sediment volume, quartz makes up a vastly larger
767 fraction of sedimentary material and thus may be a valuable source of information.
768

769

770 **Acknowledgements**

771 We thank C.A. Macris for a particularly insightful review, and two anonymous reviewers for
772 their detailed comments and suggestions which improved the content of this manuscript. We
773 also thank the handling editor Edwin Schauble for useful comments and suggestions. This work
774 was supported by NSF grants EAR-1447404 and EAR-1650033, and NERC grant
775 NE/R002134/1. DT thanks Jacob Buettner, Yanling Yang, Wriju Chowdhury, and Chis Pratt for
776 assistance. We thank the support of the analytical staff at IPGP (Julien Moureau, Pascale Louvat,
777 Delphine Limmois), where much of the measurement for this work were made, as well as Eva
778 Stueeken and Finlay Morrison for use of their furnace facilities at St Andrews. PS would also
779 like to cite the support of a Carnegie Trust Research Incentive Grant, which helped the setup of
780 various isotope techniques in the St Andrews Isotope Geochemistry (STAiG) laboratories. FM
781 thanks the ERC under the European Community's H2020 framework program/ERC grant
782 agreement # 637503 (Pristine) and for the UnivEarthS Labex program (no. ANR-10-LABX-0023
783 and ANR-11-IDEX-0005-02). Parts of this work were supported by IPGP multidisciplinary
784 program PARI, and by Region île-de-France SESAME Grant (no. 12015908).
785

786 **References**

- 787
- 788 Abraham, K., Hofmann, A., Foley, S.F., Cardinal, D., Harris, C., Barth, M.G. and André, L.
789 (2011) Coupled silicon–oxygen isotope fractionation traces Archaean silicification. *Earth
790 and Planetary Science Letters* 301, 222-230.
- 791 Ackerson, M.R., Mysen, B.O., Tailby, N.D. and Watson, E.B. (2018) Low-temperature
792 crystallization of granites and the implications for crustal magmatism. *Nature* 559, 94-97.
- 793 Ayers, J.C., Brenan, J.M., Watson, E.B., Wark, D.A. and Minarik, W.G. (1992) A new capsule
794 technique for hydrothermal experiments using the piston-cylinder apparatus. *American
795 Mineralogist* 77, 1080-1086.
- 796 Ayers, J.C. and Peters, T.J. (2018) Zircon/fluid trace element partition coefficients measured by
797 recrystallization of Mud Tank zircon at 1.5 Pa and 800-1000oC. *Geochemica et
798 Cosmochimica acta* 223, 60-74.
- 799 Ayers, J.C. and Watson, E.B. (1991) Solubility of Apatite, Monazite, Zircon, and Rutile in
800 Supercritical Aqueous Fluids with Implications for Subduction Zone Geochemistry.
801 *Philosophical Transactions of the Royal Society A: Mathematical, Physical and
802 Engineering Sciences* 335, 365-375.
- 803 Ayers, J.C. and Watson, E.B. (1993a) Apatite/fluid partitioning of rare-earth elements and
804 strontium: Experimental results at 1.0 GPa and 1000°C and application to models of
805 fluid-rock interaction. *Chemical Geology* 110, 299-314.

- 806 Ayers, J.C. and Watson, E.B. (1993b) Rutile solubility and mobility in supercritical aqueous
807 fluids. *Contrib Mineral Petrol* 114, 321-330.
- 808 Bějina, F. and Jaoul, O. (1996) Silicon self-diffusion in quartz and diopside measured by nuclear
809 micro-analysis methods *Physics of the Earth and Planetary Interiors* 97, 145-162
- 810 Bindeman, I.N., Watts, K.E., Schmitt, A.K., Morgan, L.A. and Shanks, P.W.C. (2007)
811 Voluminous low $\delta^{18}\text{O}$ magmas in the late Miocene Heise volcanic field, Idaho:
812 Implications for the fate of Yellowstone hotspot calderas. *Geology* 35, 1019-1022.
- 813 Boehnke, P., Watson, E.B., Trail, D., Harrison, T.M. and Schmitt, A.K. (2013) Zircon saturation
814 re-revisited. *Chemical Geology* 351, 324-334.
- 815 Caro, G., Morino, P., Mojzsis, S.J., Cates, N.L. and Bleeker, W. (2017) Sluggish Hadean
816 geodynamics: Evidence from coupled 146,147 Sm– 142,143 Nd systematics in
817 Eoarchean supracrustal rocks of the Inukjuak domain (Québec). *Earth and Planetary
818 Science Letters* 457, 23-37.
- 819 Cavosie, A.J., Kita, N.T. and Valley, J.W. (2009) Primitive oxygen-isotope ratio recorded in
820 magmatic zircon from the Mid-Atlantic Ridge. *American Mineralogist* 94, 926-934.
- 821 Cavosie, A.J., Valley, J.W., Wilde, S.A. and E.I.M.F (2005) Magmatic $\delta^{18}\text{O}$ in 4400–3900 Ma
822 detrital zircons: A record of the alteration and recycling of crust in the Early Archean.
823 *Earth and Planetary Science Letters* 235, 663-681.
- 824 Cawood, P.A. and Hawkesworth, C. (2019) Continental crustal volume, thickness and area, and
825 their geodynamic implications. *Gondwana Research* 66, 116–125.
- 826 Chacko, T., Cole, D.R. and Horita, J. (2001) Equilibrium oxygen, hydrogen and carbon isotope
827 fractionation factors applicable to geologic systems. *Reviews in mineralogy and
828 geochemistry* 43, 1-81.
- 829 Chappell, B.W., White, A.J.R. and Hine, R. (1988) Granite provinces and basement terranes in
830 the Lachlan Fold Belt, southeastern Australia. *Australian Journal of Earth Sciences* 35,
831 505-521.
- 832 Cherniak, D.J. (2008) Si diffusion in zircon. *Physics and Chemistry of Minerals* 35, 179-187.
- 833 Chiba, H., Chacko, T., Clayton, R.N. and Goldsmith, J.R. (1989) Oxygen isotope fractionations
834 involving diopside, forsterite, magnetite, and calcite: Application to geothermometry.
835 *Geochimica et Cosmochimica Acta* 53, 2985-2995.
- 836 Currie, K.L., Knutson, J. and Tembly, P.A. (1992) The Mud Tank carbonatite complex, central
837 Australia- an example of metasomatism at mid-crustal levels. *Contr. Mineral. and Petrol.*
838 109, 326-339.
- 839 Deng, Z., Chaussidon, M., Savage, P.S., Robert, F., Pik, R. and Moynier, F. (2019) Titanium
840 isotopes as a tracer for the plume or island arc affinity of felsic rocks. *Proc Natl Acad Sci*
841 116, 1132–1135
- 842 Ding, T. et al. (1996) *Silicon Isotope Geochemistry*, Geological Publishing, Beijing.
- 843 Ferry, J.M. and Watson, E.B. (2007) New thermodynamic models and revised calibrations for
844 the Ti-in-zircon and Zr-in-rutile thermometers. *Contributions to Mineralogy and
845 Petrology* 154, 429-437.
- 846 Frings, P., Clymans, W., Fontorbe, G., De La Rocha, C.L. and Conley, D.J. (2016) The
847 continental Si cycle and its impact on the ocean Si isotope budget. *Chemical Geology*
848 425, 12-36.
- 849 Georg, B. (2006) Geochemistry of stable silicon isotopes measured by high-resolution multi-
850 collector inductively coupled plasma mass spectrometry (HR-MC-ICPMS). Ph.D. thesis,
851 Swiss Federal Institute of Technology, Zurich.

- 852 Georg, R.B., Reynolds, B.C., Frank, M. and Halliday, A.N. (2006) New sample preparation
853 techniques for the determination of Si isotopic compositions using MC-ICPMS.
854 *Chemical Geology* 235, 95-104.
- 855 Geisler, T., Ulonska, M., Schleicher, H., Pidgeon, R.T. and van Bronswijk, W. (2001) Leaching
856 and differential recrystallization of metamict zircon under experimental hydrothermal
857 conditions. *Contributions to Mineralogy and Petrology* 141, 53-65.
- 858 Grimes, C.B., Ushikubo, T., Kozdon, R. and Valley, J.W. (2013) Perspectives on the origin of
859 plagiogranite in ophiolites from oxygen isotopes in zircon. *Lithos* 179, 48-66.
- 860 Harmon, R.S. and Hoefs, J. (1995) Oxygen isotope heterogeneity of the mantle deduced from
861 global ISO systematics of basalts from different geotectonic settings. *Contrib Mineral
862 Petrol* 120, 95-114
- 863 Harrison, T.M., Bell, E.A. and Boehnke, P. (2017) Hadean Zircon Petrochronology. *Reviews in
864 Mineralogy and Geochemistry* 83, 329–363.
- 865 Heck, P.R., Huberty, J.M., Kita, N.T., Ushikubo, T., Kozdon, R. and Valley, J.W. (2011) SIMS
866 analyses of silicon and oxygen isotope ratios for quartz from Archean and
867 Paleoproterozoic banded iron formations. *Geochimica et Cosmochimica Acta* 75, 5879-
868 5891.
- 869 Keay, S., Collins, W.J., McCulloch, M.T (1997) A three-component Sr-Nd isotopic mixing
870 model for granitoid genesis, Lachlan fold belt, eastern Australia. *Geology* 25, 307–310.
- 871 Kemp, A.I.S., Whitehouse, M.J., Hawkesworth, C.J. and Alarcon, M.K. (2005) A zircon U-Pb
872 study of metaluminous (I-type) granites of the Lachlan Fold Belt, southeastern Australia:
873 implications for the high/low temperature classification and magma differentiation
874 processes. *Contributions to Mineralogy and Petrology* 150, 230-249.
- 875 Kieffer S. W. (1982) Thermodynamics and lattice vibrations of minerals: 5. applications to
876 phase equilibria, isotopic fractionation, and high-pressure thermodynamic properties. *Rev.
877 Geophys. Space Phys.*, 20, 827-849.
- 878 Kleine, B.I., Stefánsson, A., Halldórsson, S.A., Whitehouse, M.J. and Jónasson, K. (2018)
879 Silicon and oxygen isotopes unravel quartz formation processes in the Icelandic crust.
880 *Geochemical Perspectives Letters*, 5-11.
- 881 Lackey, J.S., Valley, J.W., Chen, J.H. and Stockli, D.F. (2008) Dynamic Magma Systems,
882 Crustal Recycling, and Alteration in the Central Sierra Nevada Batholith: the Oxygen
883 Isotope Record. *Journal of Petrology* 49, 1397-1426.
- 884 Lazar, C., Young, E.D. and Manning, C.E. (2012) Experimental determination of equilibrium
885 nickel isotope fractionation between metal and silicate from 500°C to 950°C. *Geochimica
886 et Cosmochimica Acta* 86, 276-295.
- 887 Loewen, M.W. and Bindeman, I.N. (2015) Oxygen isotope and trace element evidence for three-
888 stage petrogenesis of the youngest episode (260–79 ka) of Yellowstone rhyolitic
889 volcanism. *Contributions to Mineralogy and Petrology* 170.
- 890 Loewen, M.W. and Bindeman, I.N. (2016) Oxygen isotope thermometry reveals high magmatic
891 temperatures and short residence times in Yellowstone and other hot-dry rhyolites
892 compared to cold-wet systems. *American Mineralogist* 101, 1222-1227.
- 893 Macris, C.A., Young, E.D. and Manning, C.E. (2013) Experimental determination of equilibrium
894 magnesium isotope fractionation between spinel, forsterite, and magnesite from 600 to
895 800 °C. *Geochimica et Cosmochimica Acta* 118, 18-32.

896 Mathews, A., Goldsmith, J.R., Clayton, R.N. (1983) Oxygen isotope fractionations involving
897 pyroxenes: the calibration of mineral-pair geothermometers *Geochim. Cosmochim. Acta*
898 47, 631-644.

899 Matsuhisa, Y., Goldsmith, J.R. and Clayton, R.N. (1978) Mechanisms of hydrothermal
900 crystallization of quartz at 250 C and 15 kbar. *Geochimica et Cosmochimica Acta* 42,
901 173-182.

902 Méheut, M., Lazzeri, M., Balan, E. and Mauri, F. (2009) Structural control over equilibrium
903 silicon and oxygen isotopic fractionation: A first-principles density-functional theory
904 study. *Chemical Geology* 258, 28-37.

905 Méheut, M. and Schauble, E.A. (2014) Silicon isotope fractionation in silicate minerals: Insights
906 from first-principles models of phyllosilicates, albite and pyrope. *Geochimica et*
907 *Cosmochimica Acta* 134, 137-154.

908 Mojzsis, S.J., Harrison, T.M. and Pidgeon, R.T. (2001) Oxygen-isotope evidence from ancient
909 zircons for liquid water at the Earth's surface 4,300 Myr ago. *Nature* 409, 178-181.

910 Montel, J.M. (1989) Monazite end members and solid solutions: synthesis, unit-cell
911 characteristics, and utilization as microprobe standards. *Mineralogical Magazine*, 52,
912 120-123.

913 O'Neil, J.R., and Chappell, B.W. (1977) Oxygen and hydrogen isotope relations in the
914 Berridale batholith. *J. Geol. Soc. Lond.* 133, 559-571.

915 Opfergelt, S. and Delmelle, P. (2012) Silicon isotopes and continental weathering processes:
916 Assessing controls on Si transfer to the ocean. *Comptes Rendus Geoscience* 344, 723-
917 738.

918 Page, F.Z., Fu, B., Kita, N.T., Fournelle, J., Spicuzza, M.J., Schulze, D.J., Viljoen, F., Basei,
919 M.A.S. and Valley, J.W. (2007) Zircons from kimberlite: New insights from oxygen
920 isotopes, trace elements, and Ti in zircon thermometry. *Geochimica et Cosmochimica*
921 *Acta* 71, 3887-3903.

922 Pollington, A.D., Kozdon, R., Anovitz, L.M., Georg, R.B., Spicuzza, M.J. and Valley, J.W.
923 (2016) Experimental calibration of silicon and oxygen isotope fractionations between
924 quartz and water at 250°C by in situ microanalysis of experimental products and
925 application to zoned low $\delta^{30}\text{Si}$ quartz overgrowths. *Chemical Geology* 421, 127-142.

926 Qin, T., Wu, F., Wu, Z. and Huang, F. (2016) First-principles calculations of equilibrium
927 fractionation of O and Si isotopes in quartz, albite, anorthite, and zircon. *Contributions to*
928 *Mineralogy and Petrology* 171.

929 Reynolds, B.C., Aggarwal, J., Andre, L., Baxter, D., Beucher, C., Brzezinski, M.A., Engstrom,
930 E., Georg, R.B., Land, M., Leng, M.J., Opfergelt, S., Rodushkin, I., Sloane, H.J., van den
931 Boorn, S.H.J.M., Vroon, P.Z. and Cardinal, D. (2007) An inter-laboratory comparison of
932 Si isotope reference materials. *Journal of Analytical Atomic Spectrometry* 22, 561-568.

933 Reynolds, J.H., Verhoogen, J. Natural variations in the isotopic constitution of silicon.
934 *Geochimica et Cosmochimica Acta* 1952.

935 Savage, P.S., Armytage, R.M.G., Georg, R.B. and Halliday, A.N. (2014) High temperature
936 silicon isotope geochemistry. *Lithos* 190-191, 500-519.

937 Savage, P.S., Georg, R.B., Williams, H.M., Burton, K.W. and Halliday, A.N. (2011) Silicon
938 isotope fractionation during magmatic differentiation. *Geochimica et Cosmochimica Acta*
939 75, 6124-6139.

- 940 Savage, P.S., Georg, R.B., Williams, H.M. and Halliday, A.N. (2013a) The silicon isotope
941 composition of the upper continental crust. *Geochimica et Cosmochimica Acta* 109, 384-
942 399.
- 943 Savage, P.S., Georg, R.B., Williams, H.M. and Halliday, A.N. (2013b) Silicon isotopes in
944 granulite xenoliths: insights into isotopic fractionation during igneous processes and the
945 composition of the deep continental crust. *Earth and Planetary Science Letters* 365, 221-
946 231.
- 947 Savage, P.S., Georg, R.B., Williams, H.M., Turner, S., Halliday, A.N. and Chappell, B.W.
948 (2012) The silicon isotope composition of granites. *Geochimica et Cosmochimica Acta*
949 92, 184-202.
- 950 Savage, P.S. and Moynier, F. (2013) Silicon isotopic variation in enstatite meteorites: Clues to
951 their origin and Earth-forming material. *Earth and Planetary Science Letters* 361, 487-
952 496.
- 953 Shahar, A., Ziegler, K., Young, E.D., Ricolleau, A., Schauble, E.A. and Fei, Y. (2009)
954 Experimentally determined Si isotope fractionation between silicate and Fe metal and
955 implications for Earth's core formation. *Earth and Planetary Science Letters* 288, 228-
956 234.
- 957 Spetsius, Z.V., Belousova, E.A., Griffin, W., O'Reilly, S.Y. and Pearson, N.J. (2002) Archean
958 sulfide inclusions in Paleozoic zircon megacrysts from the Mir kimberlite, Yakutia:
959 implications for the dating of diamonds *Earth and Planetary Science Letters* 199, 111-
960 126.
- 961 Taylor, H.P. (1968) The oxygen isotope geochemistry of igneous rocks. *Contrib. Mineral. Petrol.*
962 19, 1-71.
- 963 Taylor, H.P. and Sheppard, S.M.F. (1986) *Igneous Rocks: I. Processes of isotopic fractionation*
964 *and isotope systematics. Reviews in Mineralogy* 16, 227-271.
- 965 Teng, F.-Z., Li, W.-Y., Rudnick, R.L. and Gardner, L.R. (2010) Contrasting lithium and
966 magnesium isotope fractionation during continental weathering. *Earth and Planetary*
967 *Science Letters* 300, 63-71.
- 968 Thomas, J.B., Watson, E.B., Spear, F.S., Shemella, P.T., Nayak, S.K. and Lanzirrotti, A. (2010)
969 TitanQ under pressure: the effect of pressure and temperature on the solubility of Ti in
970 quartz. *Contributions to Mineralogy and Petrology* 160, 743-759.
- 971 Trail, D., Bindeman, I.N., Watson, E.B. and Schmitt, A.K. (2009) Experimental calibration of
972 oxygen isotope fractionation between quartz and zircon. *Geochimica et Cosmochimica*
973 *Acta* 73, 7110-7126.
- 974 Trail, D., Boehnke, P., Savage, P.S., Liu, M.C., Miller, M.L. and Bindeman, I. (2018) Origin and
975 significance of Si and O isotope heterogeneities in Phanerozoic, Archean, and Hadean
976 zircon. *Proc Natl Acad Sci U S A* 115, 10287-10292.
- 977 Trail, D., Tailby, N.D., Wang, Y., Harrison, T.M. and Boehnke, P. (2017) Aluminum in zircon as
978 evidence for peraluminous and metaluminous melts from the Hadean to present.
979 *Geochemistry, Geophysics, Geosystems* 10.1002/2016GC006794 1-14.
- 980 Trail, D., Thomas, J.B. and Watson, E.B. (2011) The incorporation of hydroxyl into zircon.
981 *American Mineralogist* 96, 60-67.
- 982 Valley, J.W., Bindeman, I.N. and Peck, W.H. (2003) Empirical calibration of oxygen isotope
983 fractionation in zircon. *Geochimica et Cosmochimica Acta* 67, 3257-3266.
- 984 Valley, J.W., Chiarenzelli, J.R. and McLelland, J.M. (1994) Oxygen isotope geochemistry of
985 zircon. *Earth and Planetary Science Letters* 126, 187-206.

986 Valley, J.W., Kinny, P.D., Schulze, D.J., Spicuzza, M.J. (1998) Zircon megacrysts from
987 kimberlite: oxygen isotope variability among mantle melts. *Contrib Mineral Petrol* 133,
988 1-11.
989 Watson, E. and Cherniak, D. (1997) Oxygen diffusion in zircon. *Earth and Planetary Science*
990 *Letters* 148, 527-544.
991 Watson, E. and Harrison, T. (2005) Zircon thermometer reveals minimum melting conditions on
992 earliest Earth. *Science* 308, 841-844.
993 Watson, E.B. and Harrison, T.M. (1983) Zircon saturation revisited: temperature and
994 composition effects in a variety of crustal magma types. *Earth and Planetary Science*
995 *Letters* 64, 295-304.
996 Young, E.D., Galy, A. and Nagahara, H. (2002) Kinetic and equilibrium mass-dependent isotope
997 fractionation laws in nature and their geochemical and cosmochemical significance.
998 *Geochimica et Cosmochimica Acta* 66, 1095–1104.
999

1000
1001
1002
1003
1004
1005
1006
1007
1008
1009
1010
1011

Figure Captions

1012 **Figure 1** Schematic of the experimental configuration, formed of NaCl cells surrounding
1013 borosilicate glass and a graphite furnace, which was used for all experiments. Silver capsules
1014 were machined with an outer diameter of 7.3 mm and inner diameter of 4.8 mm. Capsules were
1015 8 mm in length with a 2 mm lid. During cold pressurization, the Ag lid seals the capsule shut
1016 without requiring heating of the metal by welding (Trail et al., 2009; Thomas et al., 2010). This
1017 also results in a systematic and well-defined geometry for each experiment. The pressure media
1018 – i.e., MgO – is embedded in the exterior of the capsule during the dwell time at temperature,
1019 which means that comparing weight of capsules before and after the experiment cannot be used
1020 to assess weight loss. Additional details related to creation of a water-tight seal using the
1021 pressure-sealing technique is located elsewhere (e.g., Ayers and Watson, 1991; Ayers et al.,
1022 1992; Ayers and Watson 1993a,b).
1023

1024
1025 **Figure 2.** Schematic diagram for the three-isotope exchange method used for some experiments
1026 conducted in this study. The SiO₂ was doped off the terrestrial mass fractionation line to target
1027 $\delta^{29}\text{Si}$ and $\delta^{30}\text{Si}$ values of ~ -3 ‰ (all $\delta^x\text{Si}$ relative to NBS-28), whereas terrestrial mantle zircon
1028 was used for the starting material ($\delta^{29}\text{Si} = -0.17$ ‰, $\delta^{30}\text{Si} = -0.34$ ‰; Trail et al. 2018). Longer
1029 experiment durations led to increased isotopic exchange between the two reservoirs. The
1030 intersection of the experimental data with the secondary mass fractionation line (SMFL) is used

1031 to calculate the equilibrium fractionation. Note that in our experiments the SMFL intercept is
1032 also constrained by the mass balance.
1033

1034 **Figure 3.** Representative SEM and CL images of the starting materials and experimental
1035 products. **(a)** SE image of zircon from a direct synthesis experiment (725 °C) showing ~3 μm
1036 zircons. **(b)** Secondary electron (SE) image of crushed and ground Mud Tank zircon used as the
1037 starting material for the three-isotope method experiments. This material is representative of the
1038 size and appearance of zircons fragments added to experiments. **(c)** SE image of quartz and
1039 zircon from the “zircon fraction” for the 800 °C, 500 h experiment before HF treatment. Note
1040 the lack of angular grain fragments which is evidence that the zircon starting material underwent
1041 micron-scale recrystallization during the experiment. **(d)** SE image of zircons from an 800 °C
1042 experiment held for 500 hours, after HF treatment overnight. **(e)** Backscattered electron image
1043 of quartz grains (900 °C, 150 h) showing small micron-sized zircon inclusions circled in the
1044 image. **(f)** Cathodoluminescence image of untreated Mud Tank zircon. **(g-i)** CL image showing
1045 the changes in zircon luminescent characteristics after 20, 150, and 500 h (respectively) at 800
1046 °C. The CL features near the rims of heat-treated zircons are interpreted to represent
1047 incorporation of Dy due to recrystallization of zircon.
1048

1049
1050 **Figure 4** Average Si isotope compositions of three-isotope method experiments plotted against
1051 experiment duration. The initial composition (open symbol) is plotted at $t = 0$. The $\delta^{30}\text{Si}$
1052 averages and 2 s.d. values for each temperature series are included. These average values, which
1053 are used to constrain the isotopic composition of the system and to calculate the fractionation
1054 values, agree well with the initial composition.
1055

1056
1057 **Figure 5.** Three-isotope plots for the three different temperatures explored in this study (isotope
1058 ratios are reported relative to NBS-28). Si isotope fractionation between zircon and quartz are
1059 calculated by extrapolation to the secondary mass fractionation line (SMFL) and constrained by
1060 mass balance. The dashed lines represent 95% confidence intervals.
1061

1062 **Figure 6.** The % exchanged of zircon plotted against % exchanged quartz for individual
1063 experiments for three-isotope exchange experiments. The % exchanged is calculated by
1064 subtracting isotope composition of the starting material from the experimental product and then
1065 dividing by the total length of the isotope line whose endpoints are defined by the starting
1066 material and the extrapolated intersection of the data with the SMFL.
1067

1068 **Figure 7.** Results of experiments showing Si isotope fractionation between quartz and zircon for
1069 the three different temperatures for both experimental methods (error bars are 2 s.d.). The fit to
1070 the three-isotope data yields an A -value of 0.53 ± 0.14 (2 s.e.). Direct synthesis experiments are
1071 not included in the fit (see text for details).
1072

1073 **Figure 8.** A comparison of quartz-zircon Si isotope fractionations lines using the different A -
1074 values in Table 3. The experiment lines are derived independently from three-isotope the direct
1075 synthesis methods. The direct synthesis method is in closest agreement with the calculations of

1076 Qin et al. (2016), whereas the natural data presented in Trail et al. (2018) yield the best
1077 agreement with the three-isotope method.

1078
1079 **Figure 9.** Schematic showing the predicted relationship between $\Delta^{30}\text{Si}(\text{WR-zrc})$ as the SiO_2
1080 composition of the system decreases, because of the reduction in polymerization between
1081 crystallizing zircon and other phases. The red curve represents $\Delta^{30}\text{Si}(\text{qtz-zrc})$ calibration defined
1082 by this work ($A = 0.53$). The $\Delta^{30}\text{Si}(\text{WR-zrc})$ value, with $\text{SiO}_2 \approx 65$ wt. %, is calculated from
1083 $\delta^{30}\text{Si}(\text{zrc})$ and $\delta^{30}\text{Si}(\text{WR})$ values reported in Trail et al. (2018) for a tonalite. The mafic, or “ SiO_2
1084 ≈ 50 wt.%”, curve is estimated from the offset of Duluth Gabbro zircons from Si isotope
1085 composition of the mantle ($\delta^{30}\text{Si}(\text{BSE}) = -0.29$ ‰; Savage et al., 2014) and an estimated
1086 formation temperature of ~ 800 °C, assuming $\Delta^{30}\text{Si}(\text{WR-zrc}) \rightarrow 0$ as $T \rightarrow \infty$. Note that the two
1087 WR examples, while illustrative of the overall qualitative trend we wish to highlight, do not
1088 capture the complexities of fractional crystallization and zircon saturation in intermediate and
1089 mafic systems (Watson and Harrison, 1983; Boehnke et al., 2013).

1090
1091 **Figure 10.** Silicon-oxygen isotope fractionation concordia diagram for the zircon-quartz system.
1092 An A -value of 0.53 ± 0.14 is used to describe Si isotope fractionation and 2.33 ± 0.24 is used for O
1093 isotopes (Trail et al. 2009), the latter of which is in broad agreement with the empirical
1094 calibration reported by Valley et al. (2003). The dashed lines propagate A -value errors. The
1095 slope of the line is 4.4 ± 1.5 .

1096
1097
1098

Table 1 External standard Si isotope data

Sample name	analytical session	$\delta^{29}\text{Si}_{\text{NBS-28}}$	2 s.d.	$\delta^{30}\text{Si}_{\text{NBS-28}}$	2 s.d.	n
BHVO-2						
IPGP		-0.14 ±	0.03	-0.31 ±	0.05	17
STAiG old		-0.15 ±	0.03	-0.30 ±	0.04	14
STAiG new		-0.16 ±	0.05	-0.31 ±	0.04	8
<i>Savage et al (2014)</i>		-0.15 ±	0.04	-0.28 ±	0.03	
Diatomite						
IPGP		0.67 ±	0.01	1.29 ±	0.01	5
STAiG		0.62 ±	0.05	1.24 ±	0.06	10
<i>Reynolds et al (2007)</i>		0.64 ±	0.14	1.26 ±	0.2	

Figure 1

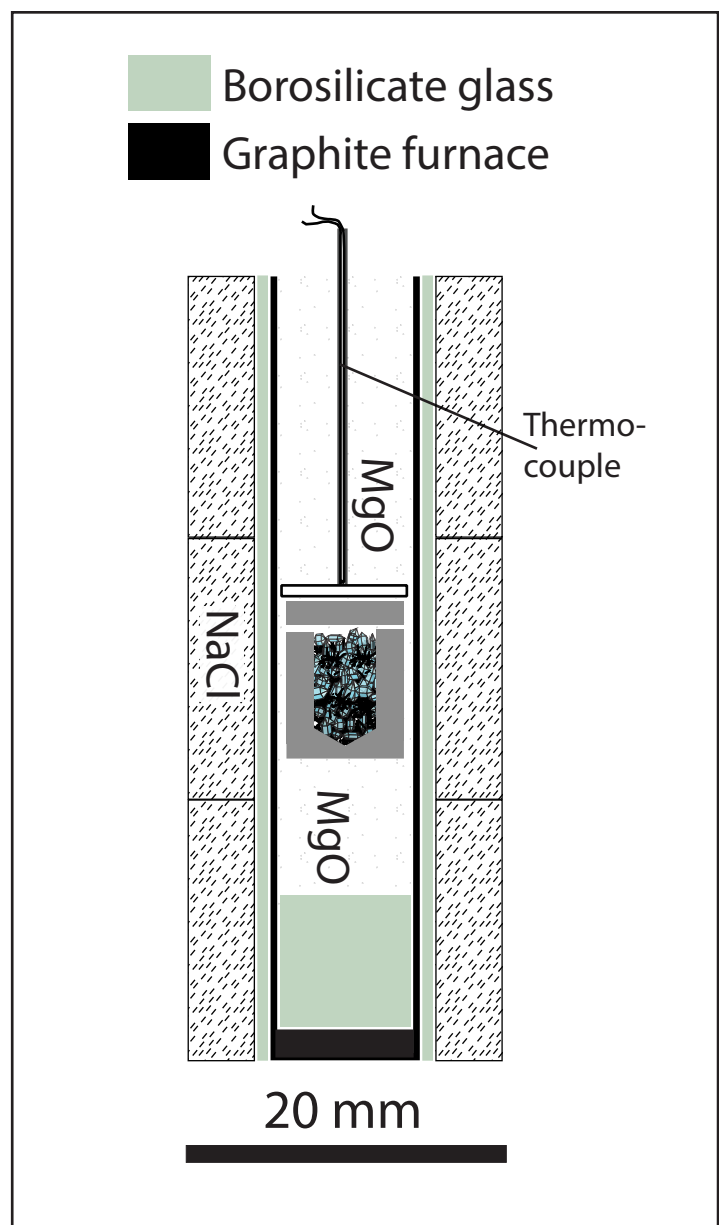


Figure 2

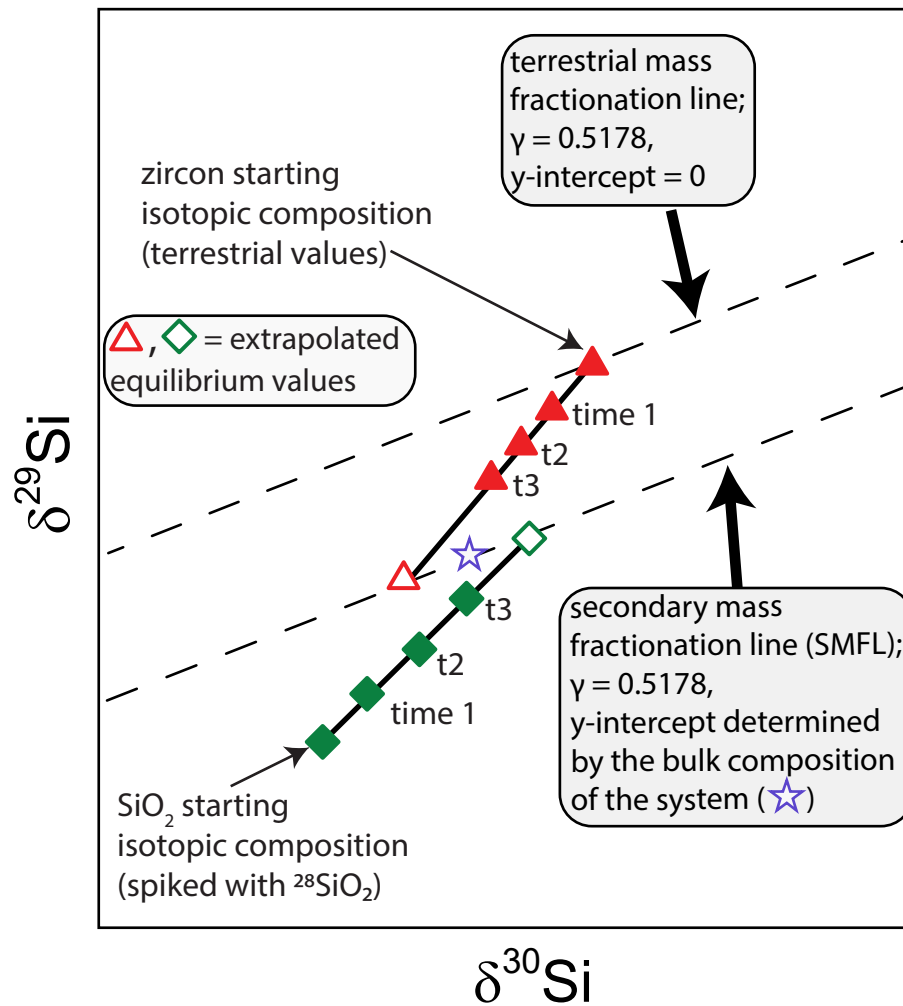


Figure 3

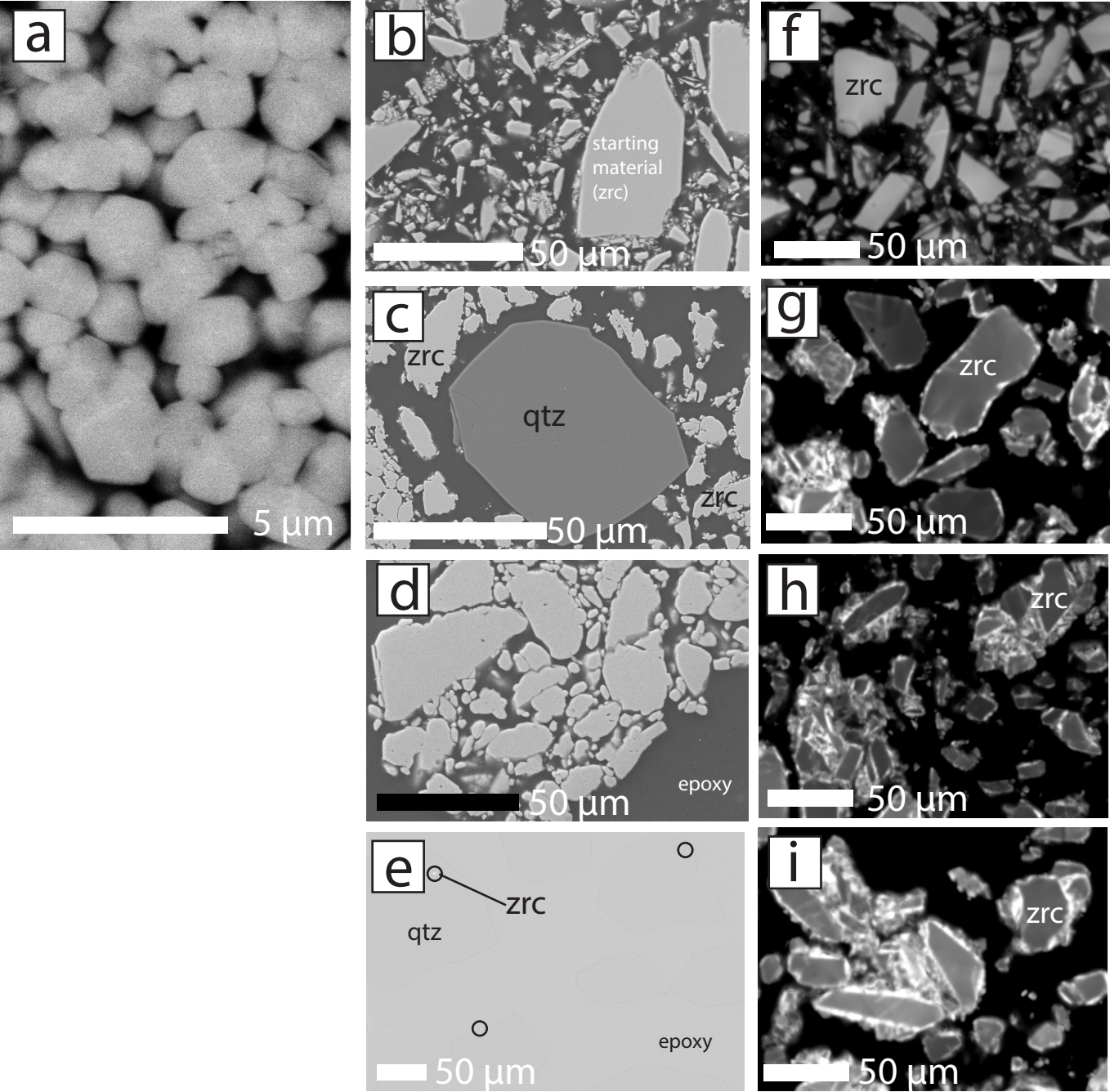


Figure 4

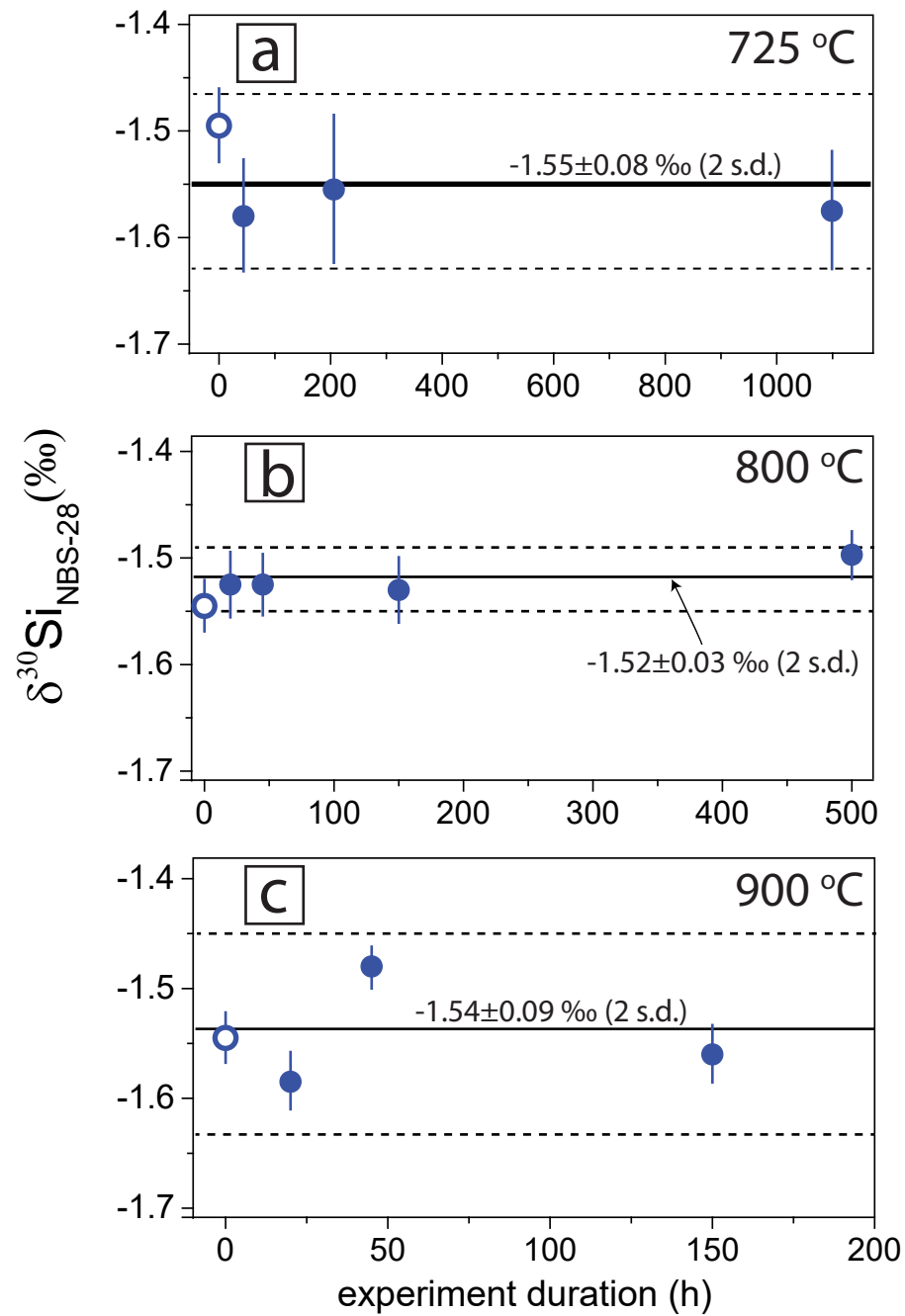


Figure 5

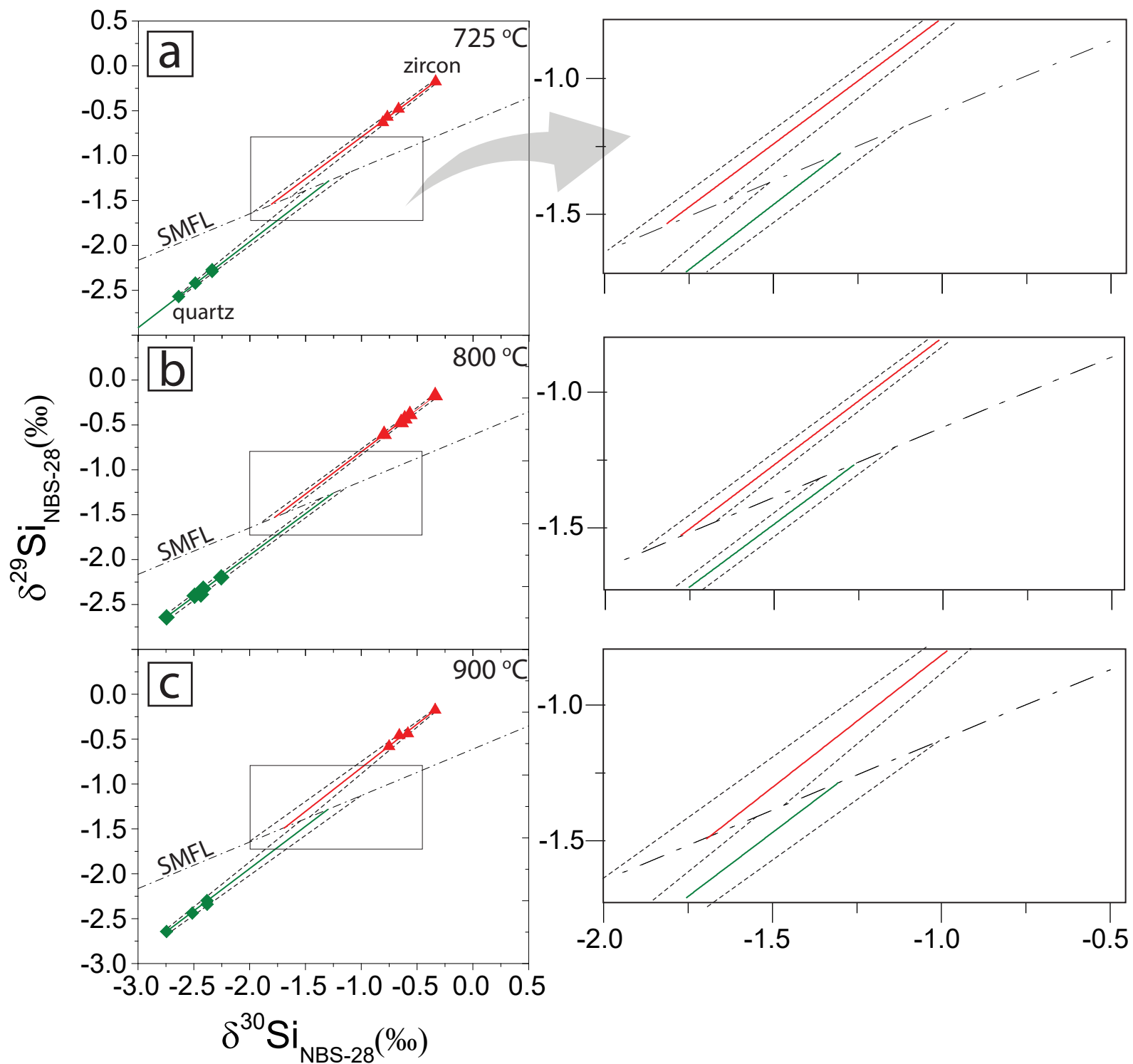


Figure 6

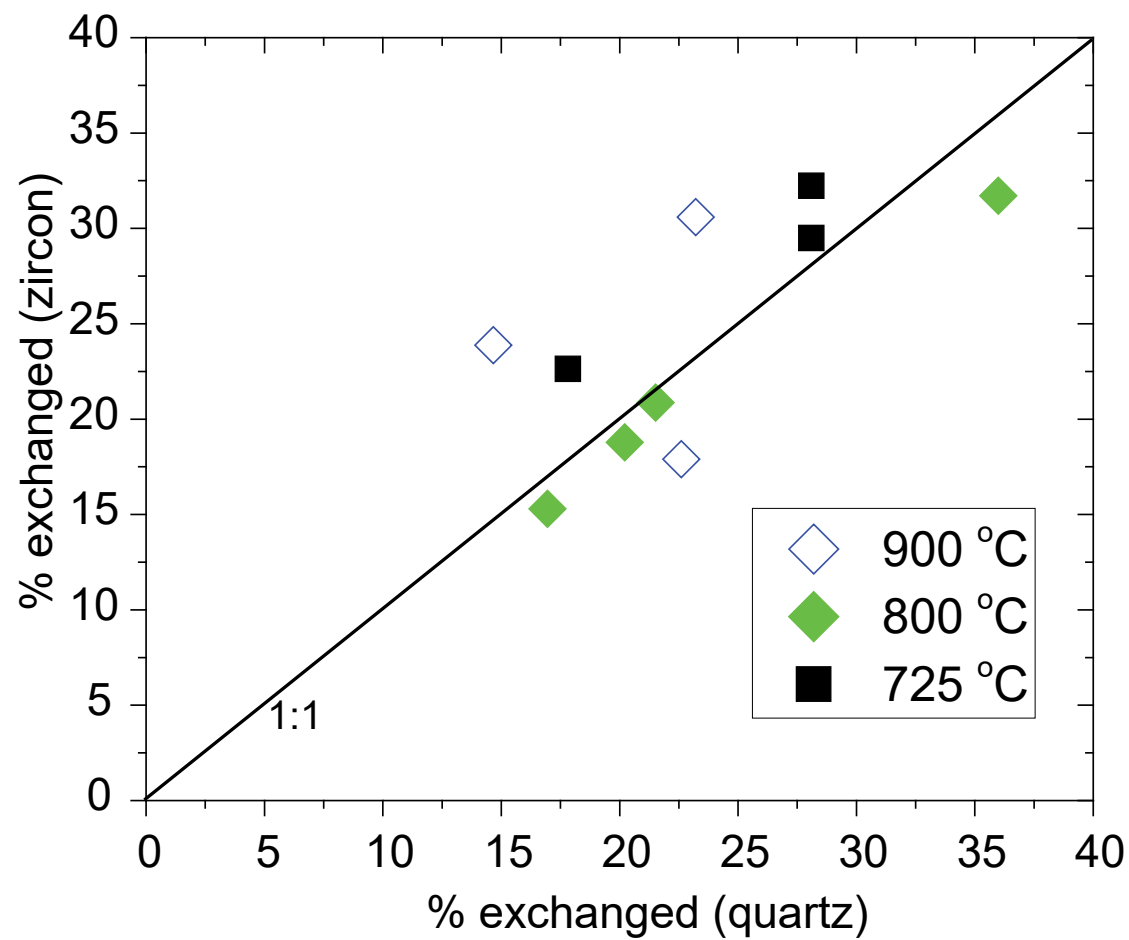


Figure 7

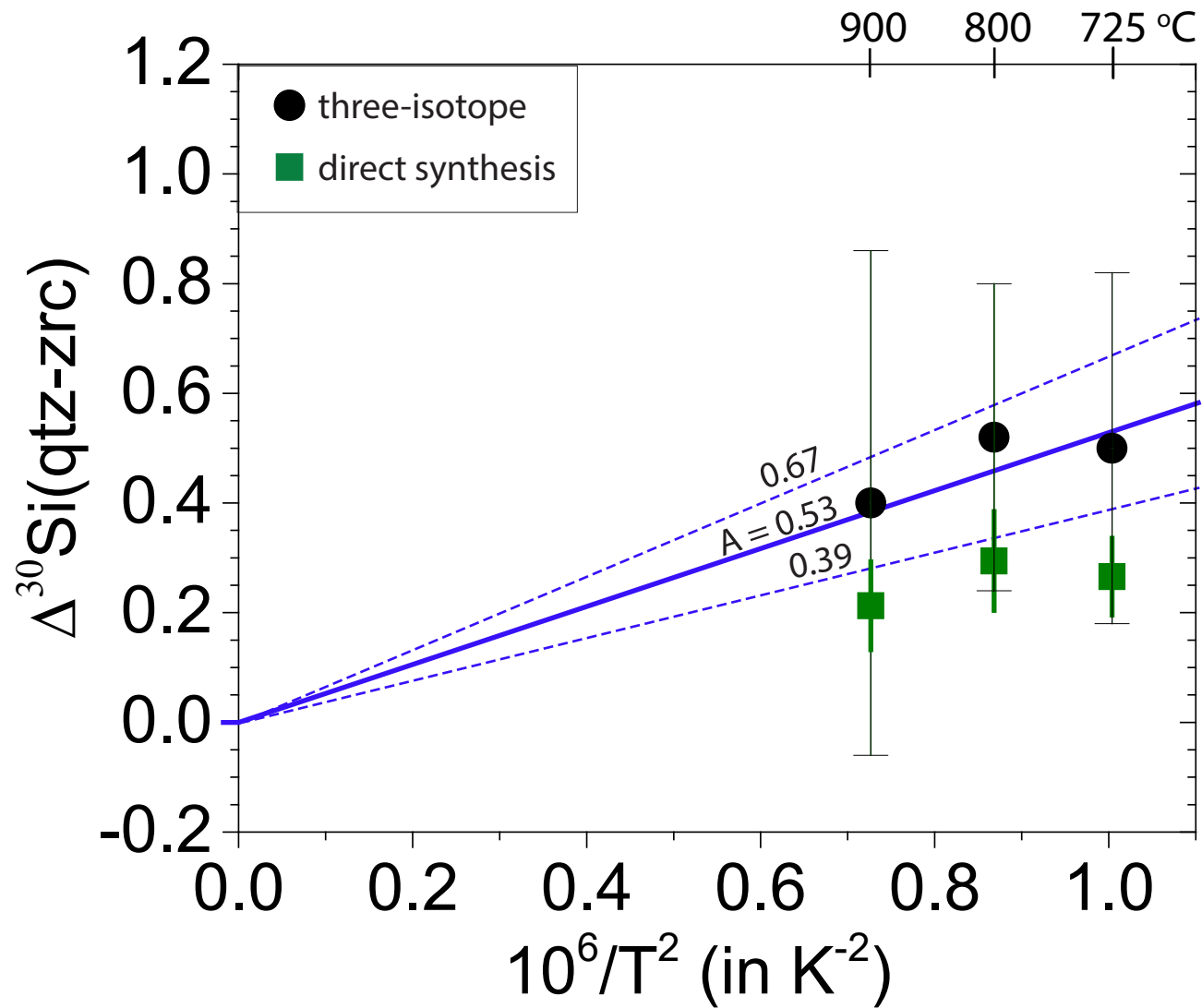


Figure 8

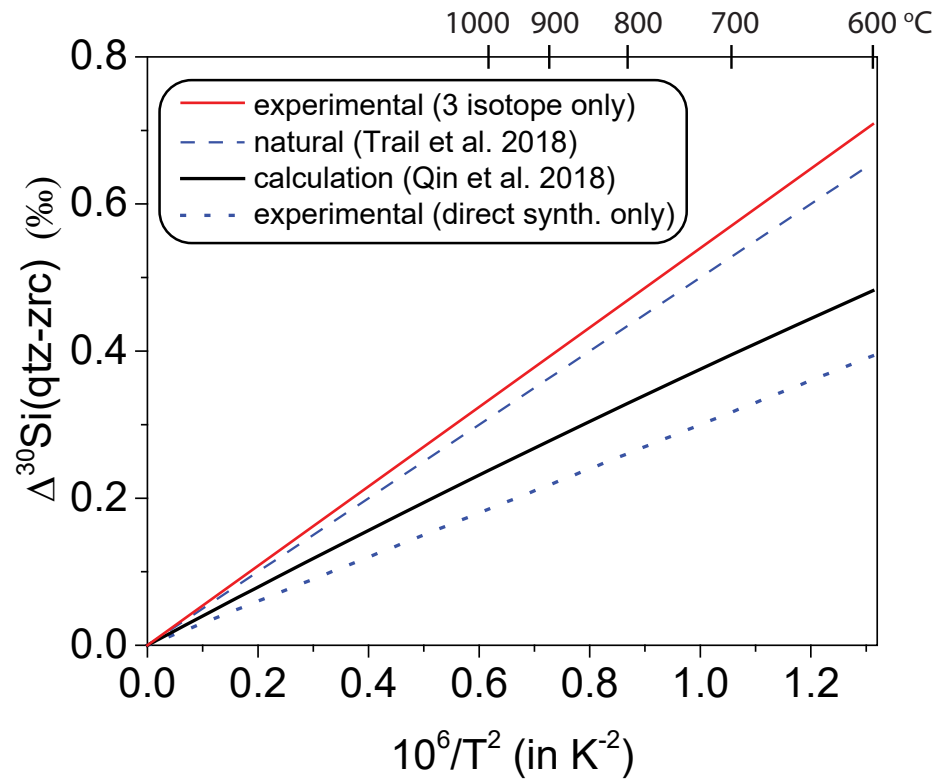


Figure 9

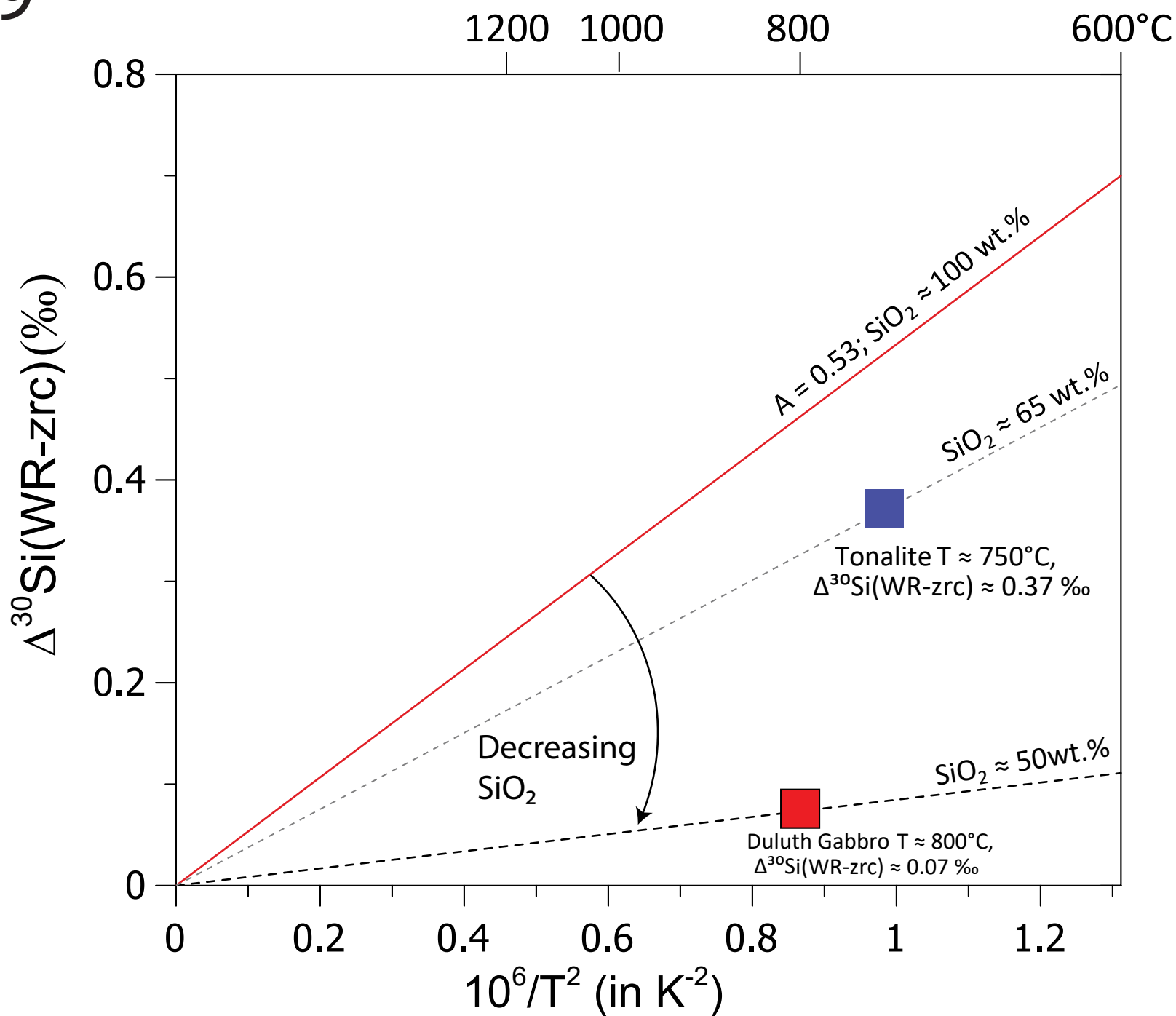


Figure 10

